

1 **The architecture of an intrusion in magmatic mush**

2

3 Alexandre Carrara^{1*}, Alain Burgisser¹, George W. Bergantz²

4

5 ¹ Univ. Grenoble Alpes, Univ. Savoie Mont Blanc, CNRS, IRD, IFSTTAR, ISTerre, 38000 Grenoble,
6 France.

7 ² Department of Earth and Space Sciences, Box 351310, University of Washington, Seattle, WA 98195,
8 USA

9

10

11 Abstract: 305 words, Main text: 5239 words, 6 Figures, 3 Tables, 50 references.

12

13

14 * Corresponding author: Email: carrara.alexandre.univ@gmail.com

15

16

17

18 **Abstract:**

19 Magmatic reservoirs located in the upper crust have been shown to result from the
20 repeated intrusions of new magmas, and spend much of the time as a crystal-rich mush. The
21 geometry of the intrusion of new magmas may greatly affect the thermal and compositional
22 evolution of the reservoir. Despite advances in our understanding of the physical processes that
23 may occur in a magmatic reservoir, the resulting architecture of the composite system remains
24 poorly constrained. Here we performed numerical simulations using a computational fluid
25 dynamics and discrete element method in order to illuminate the geometry and emplacement
26 dynamics of a new intrusion into mush and the relevant physical parameters controlling it. Our
27 results show that the geometry of the intrusion is to first order controlled by the density contrast
28 that exists between the melt phases of the intrusion and resident mush rather than the bulk density
29 contrast as is usually assumed. When the intruded melt is denser than the host melt, the intrusion
30 ponds at the base of the mush and emplaced as a horizontal layer. The occurrence of Rayleigh-
31 Taylor instability leading to the rapid ascent of the intruded material through the mush was
32 observed when the intruded melt was lighter than the host one and was also unrelated to the bulk
33 density contrast as considered before. In the absence of density contrasts between the two melt
34 phases, the intrusion may fluidize the host crystal network and slowly ascend through the mush.
35 The effect of the viscosity contrast between the intruded and host materials was found to have a
36 lesser importance on the architecture of intrusions in a mush. Analyzing the eruptive sequence of
37 well documented eruptions involving an intrusion as the trigger shows a good agreement with our

38 modeling results, highlighting the importance of specifically considering granular dynamics when
39 evaluating magmas and mush physical processes.

40 **Keywords:** Mush, Magma, Intrusion, Density contrast, CDF-DEM, Granular mechanics.

41

42 **Introduction:**

43 Evidence for injections of new magmas, also called recharge events, are ubiquitous in
44 magmatic systems (Wiebe, 2016). They are inferred to cause the formation of long-lived,
45 supersolidus magmatic reservoirs located in the upper crust (e.g. Annen et al., 2015, 2006; Dufek
46 and Bergantz, 2005; Karakas et al., 2017). Together with the thermal structure of the upper crust
47 and the frequency of recharge, the geometry and mode of emplacement of the intruded magma
48 was also identified as having a crucial effect on the long-term evolution of igneous bodies
49 (Annen et al., 2015). Diverse evidence supports the view that magmatic reservoirs reside most
50 time in a mush state that is frequently disturbed by injection of new magmas (e.g. Bachmann and
51 Huber, 2016; Cashman et al., 2017, and reference therein). A magmatic mush is a crystal-rich
52 magma in which crystals are in close and sometimes frictional contacts, forming a semi-rigid
53 framework where stress is transmitted by force chains (Bergantz et al., 2017). As a result, mushes
54 transition between crystal-rich suspensions to a 'lock-up' state that inhibits the ability of the
55 magma to erupt.

56 The injection of hotter magma into a cooler host has been suggested as a means to trigger
57 volcanic eruptions (e.g. Caricchi et al., 2014) and the intrusion style plays a fundamental role in
58 the way mush rejuvenates (process of recycling the mush to generate an eruptible magma) prior
59 to eruption (Parmigiani et al., 2014, and references therein). Several scenarios assume that the
60 intruder is emplaced as sills at the base of the mush, and rejuvenate it by supplying heat but no
61 mass except possibly exsolved volatiles (Bachmann and Bergantz, 2006; Bergantz, 1989;
62 Burgisser and Bergantz, 2011; Couch et al., 2001; Huber et al., 2011). Other scenarios consider

64 that the injected magma may penetrate the mush, producing various degrees of mixing with the
65 resident mush depending on its buoyant acceleration (e.g. Bergantz and Breidenthal, 2001;
66 Koyaguchi and Kaneko, 2000; Weinberg and Leitch, 1998). Whether an intrusion generates
67 extensive mass transfer, or is limited to thermal exchanges between an underplated intruder and a
68 host mush is thus a key element shaping the outcome of open-system events. A major obstacle to
69 our current understanding of the formation and evolution of igneous bodies is that little is known
70 about the architecture of intrusions and controlling physical parameters.

71 Traditionally, mush rejuvenation scenarios have been based on the results of experiments
72 performed with pure fluids mimicking the bulk physical properties (density and viscosity) of the
73 magmas (e.g. Huppert et al., 1986; Jellinek and Kerr, 1999; Snyder and Tait, 1995). Mush
74 dynamics, however, differs from that of pure fluids because of the complex rheological feedbacks
75 between melt and crystals. An essential physical process is that melt and crystals may experience
76 relative motions. Numerical simulations explicitly accounting for such decoupled motions as well
77 as the building and destruction of force chains between crystals (Bergantz et al., 2015; Schleicher
78 et al., 2016; Schleicher and Bergantz, 2017) have revealed that the local injection of pure melt of
79 the same density and viscosity as the mush interstitial melt easily fluidizes, penetrates, and
80 partially mixes with the overlying mush if it is sufficiently vigorous. This local unlocking of a
81 mush suggests that the conditions of efficient mass transfer and mixing are easier to achieve than
82 previously thought. Conversely, it is adding constraints on rejuvenation scenarios based on the
83 emplacement of an underlying mafic gravity current (e.g. Bachmann and Bergantz, 2006;

84 Burgisser and Bergantz, 2011) by suggesting that underplating may require contrasts in densities
85 and/or viscosities to hinder fluidization.

86 Our capacity to interpret the various natural expressions of open-system events, such as
87 eruptive products containing both the intruded magma and the resident mush, is hindered by our
88 partial understanding of the architectural end-members of these events, such as fluidization or
89 underplating. To characterize the geometry and emplacement styles of intrusion events into a
90 residing mush, we performed numerical simulations using a combination of fluid mechanics and
91 discrete elements (Bergantz et al., 2015; Schleicher et al., 2016; Schleicher and Bergantz, 2017) .
92 As the dissimilarities between the density and viscosity of the two melts require special attention
93 to better characterize the end-member cases of open-system events, we explored how these
94 parameters condition the dynamics of the intruded material when injected into a mush. We first
95 introduce the numerical model and the dimensionless parameters controlling recharge dynamics
96 that are varied in the simulations. Results of numerical simulations involving magmas of
97 contrasted physical properties are then presented in the framework of the dimensionless
98 parameters. Finally, we relate our results to well-documented cases of eruptions triggered by an
99 intrusion event.

100

101 **2: Method**

102 In order to characterize the geometry and emplacement mechanism of intrusion in mush
103 accounting for granular dynamics, we performed Computational-Fluid-Dynamic and Discrete-

104 Element-Method (CFD-DEM) numerical simulations by using the MFIX-DEM software ([https://](https://mfix.netl.doe.gov/)
 105 mfix.netl.doe.gov/). Details about the theory and implementation of the model can be found in
 106 Garg et al. (2012), Syamlal (1998), Syamlal et al. (1993), and validation of the DEM approaches
 107 in Garg et al. (2012) and Li et al. (2012) (see supplementary information 1 for a list of the
 108 equations we used). To ensure stability and efficiency of the simulations, we used the composite
 109 implicit force, which includes gravitational, pressure and drag forces, proposed by Burgisser et al.
 110 (in review) instead of the usual numerical forces evaluations (Garg et al., 2012). The composite
 111 force expression do not requires the use of time steps shorter than the characteristic durations of
 112 the hydrodynamic processes accounted. As a result, the viscosity of the melt phases may be
 113 increased without decreasing the simulation time step compared to that required to ensure the
 114 stability of a dry (zero viscosity) granular simulations.

115 The computational domain is a 3D medium of $1.6 \times 0.8 \times 0.05$ m (length \times height \times
 116 width) filled with a resident mush (Fig. 1). This geometry also allowed us to populate the mush
 117 with mm-size particles, thereby ensuring a 1:1 scale compared to nature. We will show a
 118 posteriori that our particle bed behaves identically to a bed twice as thick (Bergantz et al., 2015).
 119 Our runs are thus representative of an open system event despite the small size of the domain
 120 compared to a natural system. We used such geometry instead of a two dimensional one to ensure
 121 that the build-up and breaking of force chains have a sufficient degree of freedom in space to
 122 replicate best the mechanics of the granular phase. We created a mush layer of ~ 0.3 m height
 123 with an initial crystal content of ~ 0.64 by simulating the settling of the particles in a vacuum and
 124 positioning them at the base of the domain. We used the same density for all particles ($\rho_p = 3300$

125 kg m⁻³) and three different diameters (4.5, 5, and 5.5 mm) to avoid artificial clustering. All
126 simulations use the same initial particle bed. A crystal-free magma is injected at the base of the
127 mush layer with a superficial vertical velocity, U_{inj} , through an inlet having a width, W_{inj} . The
128 density and the viscosity of the injected melt are kept constant between all the simulations (
129 $\rho_i=2500$ kg m⁻³; $\eta_i=1$ Pa s, see table 2 for the list of the parameters kept constant). We used a
130 conduit of 3.2 cm in height to supply the inlet to ensure that the intruder enters the mush as a
131 Poiseuille flow. At the top of the domain, we used a pressure outflow boundary conditions to
132 ensure the overall mass conservation within the entire domain, which is consistent with an open-
133 system event. The boundary conditions at the front and back of the domain are cyclical, which
134 means that the intruder corresponds to a dyke having one infinite dimension. All the other
135 boundary conditions are non-slip walls (Fig 1). To maintain constant values of melt density and
136 viscosity during the runs (and hence constant density and viscosity contrasts), thermal effects are
137 ignored. This is consistent with the small dimensions of the computational domain that ensure run
138 times shorter than those allowing significant heat exchanges.

139 We performed simulations by varying the density and viscosity of the host melt. In order
140 to compare simulations, we used dimensionless quantities to scale the effects of the contrasts in
141 densities and viscosities, and injection velocities. The injection velocity and melt viscosity
142 control the stress applied by the input of new materials to the mush. These parameters enter the
143 minimum fluidization velocity, U_{mf} (Schleicher et al., 2016, see supplementary information 2 for
144 derivation of U_{mf}), which expresses the minimum superficial velocity required for the injection to
145 entrain the host solids and generate the fluidization of the particle bed. As the injected melt

146 differs from the host melt, two minimum fluidization velocities can be calculated depending on
 147 which melt is considered. For all simulations, we used the minimum of these two velocities,
 148 which here always corresponds to that using the host melt properties. The dimensionless injection
 149 velocity, U^* , is defined as:

$$150 \quad U^* = \frac{U_{inj}}{U_{mf}}. \quad (1)$$

151 In simulations having identical U^* , the injection imposes the same stress to the overlying mush.
 152 However, the time needed to inject the same new melt volume changes between simulations
 153 because U_{mf} varies. We thus used a dimensionless time, t^* , to scale the simulation time (Bergantz
 154 et al., 2017):

$$155 \quad t^* = \frac{t U_{inj}}{H_{bed}}, \quad (2)$$

156 where t is the simulation time. In this way, simulations having identical t^* implies that the same
 157 volumes of intruder have been injected until that dimensionless time and simulation results can
 158 be compared directly. The density contrast between the two materials is scaled using the reduced
 159 buoyancy of the intruder. A negative reduced buoyancy indicates that the intruder is buoyant
 160 compared to the mush, whereas a positive one indicates a tendency to sink. Two reduced
 161 buoyancies may be defined. The first one, ρ^* , expresses the buoyancy contrast between the two
 162 melts:

$$163 \quad \rho^* = \frac{\rho_i - \rho_h}{\rho_i}, \quad (3)$$

164 where ρ_i is the density of the intruded melt, and ρ_h is the host melt density. The second one, ρ_b^* ,
 165 takes the presence of crystals in the host material into account and scales the bulk densities:

$$166 \quad \rho_b^* = \frac{\rho_i - (\rho_h(1 - \Phi) + \rho_p \Phi)}{\rho_i}, \quad (4)$$

167 where ρ_p is the density of the host solids, and Φ is the particle volume fraction. The viscosity
 168 contrast, η^* , between the two melts is expressed as:

$$169 \quad \eta^* = \frac{\eta_h}{\eta_i}, \quad (5)$$

170 where η_h is the host dynamic viscosity and η_i is that of the injected melt.

171

172 **3: Results**

173 We performed 25 numerical simulations to explore the influence of the host melt density
 174 and viscosity (See Table 3 for a list of all the simulations and corresponding parameters). For
 175 these simulations, the injection velocities are such that the ratio with the respective minimum
 176 fluidization velocity, U^* , remains constant at $U^*=21.2$. This ratio is chosen to match that used
 177 previously in similar works (Schleicher et al., 2016; Schleicher and Bergantz, 2017) according to
 178 the formula presented in the supplementary material 2. We performed an additional 4 simulations
 179 at higher injection velocities to explore the effect of U^* on intrusion dynamics.

180 Figure 2 plots the simulations at the lowest U^* , 21.2, as functions of the dimensionless
181 quantities ρ^* , ρ_b^* , and η^* . It shows that the intrusions can be classified in three regimes as a
182 function of the reduced buoyancy between the two melts, ρ^* . When $\rho_i = \rho_h$, the *fluidization*
183 regime is observed. If $\rho_i > \rho_h$, the *spreading* regime occurs, whereas if $\rho_i < \rho_h$, the *rising* regime
184 occurs (see next paragraph for a detailed description of the regime dynamics). The bulk density
185 contrast ρ_b^* is always negative and the regime transition occurs at a value (-0.2025) of no
186 particular physical significance. The three regimes do not depend on the viscosity contrast η^* .

187 The *fluidization* regime was observed in the simulations once $\rho_i = \rho_h$, and consists in the
188 development of a fluidized area above the inlet in which the intruded melt rises through the mush
189 (Fig. 3A-C), as described previously (Bergantz et al., 2015; Schleicher et al., 2016). The
190 fluidization of the mush is initiated by the dilation of the crystal framework to crystal volume
191 fraction below 0.3 above the inlet that locally destabilizes the forces chains network that supports
192 the bed and separates the crystals in contact. The fluidized volume grows vertically above the
193 inlet because of two mechanisms. The first is the upward entrainment of the particles localized
194 above the fluidized cavity, which results in bulging the top surface of the mush layer (Fig. 3A-
195 C). The second mechanism is the progressive erosion of the crystals jammed at the boundary
196 between the mush and the fluidized volume. Once separated, crystals start settling in the fluidized
197 area because of this process of mush erosion, causing the fluidized area to ascend faster than the
198 intruded melt (green outline in Fig 3A-C). The intruder flows mainly vertically with a minor
199 lateral porous flow. When the fluidized cavity reaches the top of the particle bed, its width

200 progressively decreases to stabilize in the shape of a vertical chimney. At steady state, when $t^* > 1$,
201 the crystals located within the chimney show both upward and downward motions whereas the
202 ones located around the chimney flow slowly in the direction of the inlet, forming a ‘mixing
203 bowl’ as a whole, fully recovering the dynamics first described in Bergantz et al. (2015).

204 The *spreading* regime, which prevails in simulations once $\rho_i > \rho_h$, is characterized by the
205 lateral spreading of the injected melt similarly to a gravity current hugging the floor of the host
206 reservoir (Fig. 3D-F). The main difference with a pure fluid gravity current is that the melt is
207 progressively flowing across the mush as permeable flow. At the start of the injection, the crystal
208 framework experienced a dilation, which initiates host crystals settling in the same fashion as in
209 the *fluidization* regime. The lateral flow of the intruded melt is able to laterally entrain the host
210 crystals, creating two counter rotating granular vortexes in the residing mush with downward
211 motions above the inlet (Fig. 3D-F). Such granular vorticity affects the flow pattern of the fluid
212 in the mush. The fluidized volume grows either predominantly laterally or vertically, depending
213 on the relative importance between the lateral entrainment of the host solids by the intruder and
214 the vertical settling of the mush crystals. As the lateral propagation of the intruder progresses, so
215 does the size of the two granular vortexes, making this style of intrusion affect a larger mush
216 volume than the *fluidization* regime.

217 The *rising* regime (Fig. 3G-I), is characterized by the ascent of the intruded melt within
218 the mush that occurred in simulations once $\rho_i < \rho_h$. Runs start with the initial growth above the
219 inlet of a cavity filled with the intruded fluid. The cavity becomes gravitationally unstable and
220 ascends within the mush, forming a Rayleigh-Taylor instability. The ascent of the intruder

221 continues above the particle bed, entraining solids from the host. The instability is driven by its
222 head because of the buoyant batch of intruded melt. This driving batch is surrounded by a volume
223 of fluidized host mush (Fig. 3G-I). The dimensionless time at which the intrusion reaches the
224 mush top ($t^* \sim 0.3$) is shorter than that of the two other regimes because the Rayleigh-Taylor
225 instability significantly accelerates the transport of the intruder.

226 Figure 2 suggests that the viscosity contrast does not control the end-member shape of the
227 intruder flow. Larger viscosity contrasts, however, increase the trends of some aspects of mush
228 dynamics. Figure 3 illustrates how viscosity bears on flow patterns.

229 In the *fluidization* regime, the increase of the host viscosity enhances the formation of
230 crystal-poor batches at the top of the intruded volume (Fig. 3A-C). Because the minimum
231 fluidization velocity within the intruded melt is lower than for the host, the crystals are not
232 fluidized and sediment in the intruded melt to accumulate atop the inlet (Fig 3B-C). Because we
233 defined t^* to scale the dynamics of the mush, the increase of the host melt viscosity decreases the
234 injection velocity and the duration, t , required to reach the dimensionless time $t^*=1$. As a result,
235 increasing melt viscosity increases the ability for the intruded melt to experience lateral porous
236 flow through the host crystal frameworks (Fig. 3B-C). It also lengthens the time span for a
237 crystal to settle over the same characteristic distance between the intruded and host melts, which
238 results in the formation of the crystal poor volume at the top of the intruded volume (Fig. 3B-C).
239 The increase in the host melt viscosity, however, does not affect the volume of mush showing a
240 decrease in crystal volume fraction and a distortion of the force chains.

241 In the *spreading* regime, high viscosity contrasts enhance the lateral spreading of the
242 intruder and the entrainment of the host crystals in the two counter rotating vortexes (Fig 3E-F).
243 Large host melt viscosity causes the lateral entrainment of the solids to be more efficient than
244 particle settling, which results in the elongation of the fluidized volume in the horizontal
245 direction. In the same fashion as in the *fluidization* regime, the lower superficial injection rate
246 enhances the ability of the lateral porous flow of the intruder. This effect is expressed by the
247 decrease of the thickness of the intruded layer with the increase of the host viscosity (Fig 3D-F).
248 It results that reaching the same volume of mush entrained by the intrusion requires less intruded
249 material as the viscosity of the host melt increases.

250 In the *rising* regime, increasing the viscosity contrast enlarges the vortexes sizes and the
251 separation distance between their centers (Fig 3G-I). The dimensionless time, t^* , at which the
252 intruder instability occurs decreases with the viscosity of the host. The volume of the intruded
253 melt driving the Rayleigh-Taylor instabilities is lower when a viscosity contrast exists. When a
254 viscosity contrast is present, the volume of the intruded driving the instability does not vary
255 significantly (Fig 3H-I). The larger volume of the intruder driving the Rayleigh-Taylor instability
256 can be addressed by the ratio between the dimensional injection rate and Rayleigh-Taylor
257 growing rate. In Fig. 3G, this ratio is higher than in Fig 3H-I, and a significant volume of fluid is
258 injected during the growth and entrainment of the instability. On the contrary, in Fig 3H-I, this
259 ratio is sufficiently small so that the amount of melt injected during the growth of the instability
260 is negligible compared to the volume required to initiate it. However, the volume of the mush

261 remobilized by the intruder flow does not significantly vary with the host melt viscosity (Fig.
262 3G-I).

263 The additional 4 simulations in the spreading regime suggest that buoyancy effects
264 dominate the intruder flow up to $U^* \approx 10^5$. Figure 4 shows the temporal evolution of the height
265 reached by the intruded volume, H^* , as a function of injection rate. All injections grow purely
266 vertically at first ($t^* \leq 0.1$). As seen above, at the low injection rate of 21.2, the intrusion stalls
267 rapidly and spreads laterally (simulation A25, Fig. 4). Increasing the injection rate causes stalling
268 to occur later and higher. When $t^* > 0.2$, injection growth switches from vertical to radial. When
269 $U^* > 10^5$, the behavior of the intruder is dominated by the injection rate, which causes the radially
270 growing intrusion to reach the top of the bed at $H^* = 1$. Despite that all simulations have the same
271 intruder shape before stalling, the size of the region surrounding the intruder that is affected by
272 dilatancy increases with U^* . The highest injection rate (simulation B4 with $U^* = 10^6$) strictly
273 follows the theoretical curve for a radial growth and reaches $H^* = 1$ at $t^* \approx 2.5$, as predicted by
274 geometrical arguments (supplementary information 3).

275 The decoupling between the motions of the two phases results from processes unique to
276 granular mechanics that our discrete numerical model is able to capture. Mush dilation is key for
277 permeable melt flow to occur. The initiation of the intrusion increases the pore pressure in the
278 mush around the inlet (Fig. 5A). This overpressure progressively propagates outwards and
279 decreases the crystal volume fraction in the overlying mush (Fig. 5B). As the intrusion
280 propagates, the effect of the overpressure is supplemented with the Reynolds dilatancy generated

281 by the granular vortexes in the mush (Fig 5C). The dilation of the solid framework increases its
282 permeability of the solid framework and in turn the possibility of relative motion between the
283 crystals and the interstitial melt (Fig. 5C). This phenomenon is particularly clear in the case of the
284 rising regime. The intruder is surrounded by a volume of mush that underwent such dilation that
285 it is in the dilute regime. The contact region between the two magmas is dominated by melt–melt
286 interface interspersed with isolated crystals. As a result, entrainment is ruled by melt vorticity.
287 Efficient entrainment of two fluids with a viscosity contrast occurs only when the most viscous
288 fluid bears large levels of vorticity (Jellinek and Kerr, 1999). In our runs, the intruder melt
289 viscosity is equal or less than that of the host, and the vorticity is concentrated close to or inside
290 the intrusion (Fig. S4 in the supplementary information 4). This situation yields the weak
291 entrainment observed in the rising regime and the transition from vertical growth to spreading of
292 the intrusion melt as injection velocity decreases (Fig. 4). The concept of bulk reduced buoyancy
293 thus fails to predict the intrusion geometry for two reasons. First, it assumes the absence of
294 relative motion and thus ignores the transfer of crystals from host to intrusion. Second, in cases
295 when sufficient mush dilation occurs, entrainment is controlled by the melt–melt interface and
296 the associated density and viscosity contrasts. The interplay between pore pressure, dilation, melt
297 interface dynamics, and permeable flow controls the transport of mass within our modeled
298 magmatic reservoir.

299 **4: Comparison with natural systems**

300 To test the applicability of our results to natural cases, we gathered from the literature the
301 physical parameters of 15 eruptions involving the intrusion of new magma (Table S3–S4 in the

302 supplementary information 5). All host magmas are mushes but for a few cases that either have
303 crystal gradients in their reservoirs (Krakatau), or for which there is ambiguity on the respective
304 roles of the intruder and host magmas (Unzen, Minoan, and Katmai–Novarupta). In the studies
305 surveyed, melt viscosity and melt density of host magmas were most often directly determined
306 from eruptive products and pre-eruptive conditions such as pressure, temperature, and melt water
307 content (details on how parameters were obtained are in Table S3–S4 (see supplementary
308 information 5)).

309 The cases are organized into three categories depending on the observed eruptive
310 sequence. In the first category, the intruder was erupted first, followed by the emission of host
311 magma or a mixture of host and intruder. This category implies that the intruder magma was able
312 to efficiently penetrate and pass through the host magma. In the second category, both host and
313 intruder magmas were erupted simultaneously, with the intruder most often forming enclaves or
314 mingling structures. The last category feature cases where the mixing was so thorough that the
315 eruptive products only bear cryptic traces of the intruder, such as isolated intruder crystals
316 floating in the host or crystal disequilibrium textures.

317 Figure 6A shows the ratios of bulk viscosities and bulk densities between the intruder
318 magma and the host magma(s) for the 15 eruptions. Figure 6A contains two physically
319 meaningful thresholds, that of neutral buoyancy at the bulk density ratio of 0 and that of equal
320 viscosity at the bulk viscosity ratio of one. The three types of eruptive sequence are not sorted
321 following any of these thresholds. Figure 6B shows the same eruptions plotted as functions of
322 melt properties instead of bulk properties. Our numerical runs cover the full range of natural

323 density ratios and a more restricted range of viscosity ratios (from 1 to 10^2 vs. 10^{-1} to $<10^4$ in
324 nature). Figure 6B also shows the dividing line between rising and spreading dynamics at the
325 level of neutral buoyancy with respect to the melts. With the possible exception of two cases (see
326 *Discussion*), the Minoan eruption and the 1912 Katmai–Novarupta eruption, the *rising* regime is
327 populated by the eruptions that first ejected intruder material. This divide between cases where at
328 least some of the intruder magma had the capacity to go unscathed through the host and cases
329 where none of it escaped from host interaction is consistent with our numerical results.

330 **5: Discussion**

331 Our results are helpful to predict the behavior of an intrusion within a mush. The reduced
332 buoyancy between the two melts, ρ^* , is the parameters having a first order control on the
333 geometry of the intrusion. On the contrary, the commonly used level of neutral bulk buoyancy
334 (e.g. Huppert et al., 1986; Snyder and Tait, 1995) does not mark any particular change in
335 dynamic behavior (Fig. 2). This result illustrates that the relative motion between the solids and
336 surrounding melt is of primary importance when studying mush processes. Experiments, or
337 numerical simulations, that account of the presence of the solids or exsolved volatiles as discrete
338 entities (Barth et al., 2019; Bergantz et al., 2015; Girard and Stix, 2009; Hodge et al., 2012;
339 McIntire et al., 2019; Michioka and Sumita, 2005; Parmigiani et al., 2014; Schleicher et al., 2016;
340 Schleicher and Bergantz, 2017) are the most likely to faithfully reproduce mush dynamics.
341 Neglecting phase decoupling by considering the magma as a single-phase fluid having effective
342 properties such as bulk density or bulk viscosity will not capture the blending of crystal contents
343 between host and intruder and the simultaneous but independent evolution of the melt–melt

344 interface (Fig. 5C). This sheds light on the importance of granular mechanisms such as pore
345 pressure, dilatancy and permeable flow in shaping the end-member cases of mush intrusion.

346 We characterized the parameter ranges of a series of well-documented cases of eruptions
347 that features magma mixing, focusing on the densities and viscosities of the two end-member
348 magmas involved and on the order of the eruptive sequence. Two cases, Katmai and the Minoan
349 eruption, straddle two eruptive sequence categories because the intruders may have been
350 transported alongside (as opposed to through) the host magmas. Both cases are close to the
351 neutral buoyancy level, regardless of the scenario considered (Fig. 6B). Importantly, each
352 individual scenario is consistent with our regimes. The Katmai eruption first emitted rhyolite. The
353 Katmai scenario corresponding to a rhyolite intruding a more mafic host (Eichelberger and
354 Izbekov, 2000) is consistent with it being located in the *rising* regime. In the other scenario
355 (Singer et al., 2016), the rhyolite is part of the host reservoir, which is consistent with that
356 scenario being in the spreading regime. The Minoan scenario located in the rising regime
357 (Cadoux et al., 2014) would have indeed emitted the intruder first, but it feature a host filled by
358 low-crystallinity magma, which is at odds with our hypothesis that the host is in a mush state.
359 The other Minoan scenario (Druitt, 2014; Flaherty et al., 2018; Martin et al., 2010) involves a
360 mushy host compatible with this hypothesis and is consistent with the spreading regime that
361 hinders first emission of the intruder. The overall good agreement between the observed eruptive
362 sequences and our numerical results (Fig. 6B) constitutes a serious argument in favor of the fact
363 that open-system events are, to first order, controlled by the density contrast between the melt

364 phases of the intrusion and mush. It also suggests that injection momentum was quickly
365 exhausted, letting buoyancy control the unfolding of the event.

366 Two special natural cases can be added to the comparison between our dynamics regime
367 and natural data (Fig. 6B). The first is the 1883 eruption of Krakatau volcano (Mandeville et al.,
368 1996), which resulted from remobilization by basaltic intruder of a stratified magma chamber
369 featuring three compositions, none of them being in a mush state (andesite, dacite, and
370 rhyodacite). Evidence that the basalt intruder was erupted first comes from basaltic ashes
371 collected during the first phase of the eruption (Self, 1992). The presence of several magmas in
372 the host reservoir, however spatially distributed, causes a large uncertainty in the host properties.
373 As a result, the Krakatau eruption spans the divide between the regimes established by our
374 simulations (Fig. 6B). It is thus an inconclusive case where the intruder was erupted first. The
375 second natural case is the 1991–1995 eruption of Unzen volcano, for which the intruder could
376 have been either andesitic (Holtz et al., 2004), or basaltic (Browne et al., 2006). Regardless of its
377 composition, the intrusion caused thorough mixing and the first magma erupted was the product
378 of this mixing. If the intruder was basaltic, it was buoyant with respect to the felsic host and if it
379 was andesitic, it was denser than the host. As a result, Unzen spans the divide between the *rising*
380 and *spreading* regime (Fig. 6B). Considering that the intruder input was large (>30 wt% of the
381 eruptive products; Holtz et al., 2005), and if any credit is given to our inferences, the intruder was
382 more likely to be andesitic than basaltic because this latter composition would have been prone to
383 preserve its integrity while going through the host mush, erupting first.

384

385 **6: Conclusions**

386 This study highlights the importance of granular mechanics in mush processes, which
387 differ significantly from ones expected with purely fluid models. As expected, our simulations
388 show that when the injection velocity is high ($U^* > 10^5$), intrusion dynamics is dominated by the
389 injection momentum and the intruded cavities grow radially. When the injection velocity is below
390 this threshold, however, buoyancy controls the behavior of the intruder in an unexpected way.
391 Bulk buoyancy contrasts appear to play no role in the way the intruder flows. Instead, the density
392 contrast between the host and intruded melts exerts a first-order control on the architecture of an
393 intrusion event in a mush. When the two melt densities are identical, the intruder fluidizes the
394 mush and creates a mixing bowl, as described in Bergantz et al. (2015). When the intruded melt
395 is lighter than that of the host, it rises through the mush. Mush dilation around the intruder causes
396 the contact region between the two magmas to be dominated by melt–melt interface interspersed
397 with isolated crystals. Entrainment in this rising regime is ruled by the amount of vorticity of the
398 most viscous melt. As our in our runs the intruder melt viscosity was equal or lower than that of
399 the host, no entrainment was observed. Intruder melts denser than the host spread laterally partly
400 as permeable flows through the host mush. The lateral spreading of the intruder generates two
401 counter rotating granular vortexes with downward motions above the inlet, which maximizes the
402 volume of the mush entrained by the gravity current. In this spreading regime, the combined
403 effects of the initial pore overpressure at the inlet and the Reynolds dilatancy resulting from the
404 lateral spreading of the intruder are able to fluidize the overlying mush.

405 We tested whether the first-order effect of melt density contrast was expressed in nature.
406 We tallied 15 well-documented eruptive sequences, classifying them according to the expected
407 outcomes of the three dynamic regimes we defined. We found overall good agreement between
408 eruption sequences and our model predictions, which suggests that granular mechanisms such as
409 pore pressure, dilatancy, and permeable flow play a fundamental role in the unfolding of open-
410 system events. Granular dynamics and the decoupling of melt and crystals are thus key in shaping
411 reservoir and volcanic processes.

412

413 **Acknowledgments:**

414 All the numerical simulations presented in this paper were performed using the CIMENT
415 infrastructure (<https://ciment.ujf-grenoble.fr>), which is supported by the Rhône-Alpes region
416 (GRANT CPER07_13 CIRA: <http://www.ci-ra.org>). G.W.B. was supported by National Science
417 Foundation grants DGE-1256068, EAR-1049884 and EAR-1447266. Authors declare no
418 conflicts of interest.

419 **References:**

- 420 Annen, C., Blundy, J.D., Leuthold, J., Sparks, R.S.J., 2015. Construction and evolution of igneous bodies:
421 Towards an integrated perspective of crustal magmatism. *Lithos* 230, 206–221.
422 <https://doi.org/10.1016/j.lithos.2015.05.008>
- 423 Annen, C., Blundy, J.D., Sparks, R.S.J., 2006. The Genesis of Intermediate and Silicic Magmas in Deep
424 Crustal Hot Zones. *J Petrology* 47, 505–539. <https://doi.org/10.1093/petrology/egi084>
- 425 Bachmann, O., Bergantz, G.W., 2006. Gas percolation in upper-crustal silicic crystal mushes as a
426 mechanism for upward heat advection and rejuvenation of near-solidus magma bodies. *Journal of*
427 *Volcanology and Geothermal Research* 149, 85–102.
428 <https://doi.org/10.1016/j.jvolgeores.2005.06.002>

- 429 Bachmann, O., Huber, C., 2016. Silicic magma reservoirs in the Earth's crust. *American Mineralogist* 101,
 430 2377–2404. <https://doi.org/10.2138/am-2016-5675>
- 431 Barth, A., Edmonds, M., Woods, A., 2019. Valve-like dynamics of gas flow through a packed crystal
 432 mush and cyclic strombolian explosions. *Sci Rep* 9, 1–9. <https://doi.org/10.1038/s41598-018-37013-8>
- 433
- 434 Bergantz, G.W., 1989. Underplating and Partial Melting: Implications for Melt Generation and Extraction.
 435 *Science* 245, 1093–1095. <https://doi.org/10.1126/science.245.4922.1093>
- 436 Bergantz, G.W., Breidenthal, R.E., 2001. Non-stationary entrainment and tunneling eruptions: A dynamic
 437 link between eruption processes and magma mixing. *Geophysical Research Letters* 28, 3075–
 438 3078. <https://doi.org/10.1029/2001GL013304>
- 439 Bergantz, G.W., Schleicher, J.M., Burgisser, A., 2017. On the kinematics and dynamics of crystal-rich
 440 systems. *J. Geophys. Res. Solid Earth* 122, 2017JB014218. <https://doi.org/10.1002/2017JB014218>
- 441 Bergantz, G.W., Schleicher, J.M., Burgisser, A., 2015. Open-system dynamics and mixing in magma
 442 mushes. *Nature Geosci* 8, 793–796. <https://doi.org/10.1038/ngeo2534>
- 443 Browne, B.L., Eichelberger, J.C., Patino, L.C., Vogel, T.A., Uto, K., Hoshizumi, H., 2006. Magma
 444 mingling as indicated by texture and Sr/Ba ratios of plagioclase phenocrysts from Unzen volcano,
 445 SW Japan. *Journal of Volcanology and Geothermal Research, Modern Trends in Petrography*:
 446 154, 103–116. <https://doi.org/10.1016/j.jvolgeores.2005.09.022>
- 447 Burgisser, A., Bergantz, G.W., 2011. A rapid mechanism to remobilize and homogenize highly crystalline
 448 magma bodies. *Nature* 471, 212–215. <https://doi.org/10.1038/nature09799>
- 449 Burgisser, A., Carrara, A., Annen, C., in review. Numerical simulations of magmatic enclave deformation.
 450 *Journal of Volcanology and Geothermal Research* (submitted).
- 451 Cadoux, A., Scaillet, B., Druitt, T.H., Deloule, E., 2014. Magma Storage Conditions of Large Plinian
 452 Eruptions of Santorini Volcano (Greece). *J Petrology* 55, 1129–1171.
 453 <https://doi.org/10.1093/petrology/egu021>
- 454 Caricchi, L., Annen, C., Blundy, J., Simpson, G., Pinel, V., 2014. Frequency and magnitude of volcanic
 455 eruptions controlled by magma injection and buoyancy. *Nature Geoscience* 7, 126–130.
 456 <https://doi.org/10.1038/ngeo2041>
- 457 Cashman, K.V., Sparks, R.S.J., Blundy, J.D., 2017. Vertically extensive and unstable magmatic systems:
 458 A unified view of igneous processes. *Science* 355, eaag3055.
 459 <https://doi.org/10.1126/science.aag3055>
- 460 Coombs, M.L., Gardner, J.E., 2001. Shallow-storage conditions for the rhyolite of the 1912 eruption at
 461 Novarupta, Alaska. *Geology* 29, 775–778. [https://doi.org/10.1130/0091-7613\(2001\)029<0775:SSCFTR>2.0.CO;2](https://doi.org/10.1130/0091-7613(2001)029<0775:SSCFTR>2.0.CO;2)
- 462
- 463 Couch, S., Sparks, R.S.J., Carroll, M.R., 2001. Mineral disequilibrium in lavas explained by convective
 464 self-mixing in open magma chambers. *Nature* 411, 1037–1039. <https://doi.org/10.1038/35082540>
- 465 Druitt, T.H., 2014. New insights into the initiation and venting of the Bronze-Age eruption of Santorini
 466 (Greece), from component analysis. *Bull Volcanol* 76, 794. <https://doi.org/10.1007/s00445-014-0794-x>
- 467
- 468 Dufek, J., Bergantz, G.W., 2005. Lower Crustal Magma Genesis and Preservation: a Stochastic
 469 Framework for the Evaluation of Basalt–Crust Interaction. *J Petrology* 46, 2167–2195.
 470 <https://doi.org/10.1093/petrology/egi049>
- 471 Eichelberger, J.C., Izbekov, P.E., 2000. Eruption of andesite triggered by dyke injection: contrasting cases
 472 at Karymsky Volcano, Kamchatka and Mt Katmai, Alaska. *Philosophical Transactions of the*
 473 *Royal Society of London. Series A: Mathematical, Physical and Engineering Sciences* 358, 1465–
 474 1485.

- 475 Flaherty, T., Druitt, T.H., Tuffen, H., Higgins, M.D., Costa, F., Cadoux, A., 2018. Multiple timescale
476 constraints for high-flux magma chamber assembly prior to the Late Bronze Age eruption of
477 Santorini (Greece). *Contrib Mineral Petrol* 173, 75. <https://doi.org/10.1007/s00410-018-1490-1>
- 478 Garg, R., Galvin, J., Li, T., Pannala, S., 2012. Open-source MFIX-DEM software for gas–solids flows:
479 Part I—Verification studies. *Powder Technology* 220, 122–137.
- 480 Girard, G., Stix, J., 2009. Buoyant replenishment in silicic magma reservoirs: Experimental approach and
481 implications for magma dynamics, crystal mush remobilization, and eruption. *J. Geophys. Res.*
482 114, B08203. <https://doi.org/10.1029/2008JB005791>
- 483 Hammer, J.E., Rutherford, M.J., Hildreth, W., 2002. Magma storage prior to the 1912 eruption at
484 Novarupta, Alaska. *Contributions to Mineralogy and Petrology* 144, 144–162.
- 485 Hodge, K.F., Carazzo, G., Jellinek, A.M., 2012. Experimental constraints on the deformation and breakup
486 of injected magma. *Earth and Planetary Science Letters* 325–326, 52–62.
487 <https://doi.org/10.1016/j.epsl.2012.01.031>
- 488 Holtz, F., Sato, H., Lewis, J., Behrens, H., Nakada, S., 2004. Experimental petrology of the 1991–1995
489 Unzen dacite, Japan. Part I: phase relations, phase composition and pre-eruptive conditions.
490 *Journal of petrology* 46, 319–337.
- 491 Huber, C., Bachmann, O., Dufek, J., 2011. Thermo-mechanical reactivation of locked crystal mushes:
492 Melting-induced internal fracturing and assimilation processes in magmas. *Earth and Planetary*
493 *Science Letters* 304, 443–454. <https://doi.org/10.1016/j.epsl.2011.02.022>
- 494 Huppert, H.E., Sparks, R.S.J., Whitehead, J.A., Hallworth, M.A., 1986. Replenishment of magma
495 chambers by light inputs. *Journal of Geophysical Research: Solid Earth* 6113–6122.
496 [https://doi.org/10.1029/JB091iB06p06113@10.1002/\(ISSN\)2169-9356.OPENSYS1](https://doi.org/10.1029/JB091iB06p06113@10.1002/(ISSN)2169-9356.OPENSYS1)
- 497 Jellinek, A.M., Kerr, R.C., 1999. Mixing and compositional stratification produced by natural convection:
498 2. Applications to the differentiation of basaltic and silicic magma chambers and komatiite lava
499 flows. *Journal of Geophysical Research: Solid Earth* 104, 7203–7218.
500 <https://doi.org/10.1029/1998JB900117>
- 501 Karakas, O., Degruyter, W., Bachmann, O., Dufek, J., 2017. Lifetime and size of shallow magma bodies
502 controlled by crustal-scale magmatism. *Nature Geoscience* 10, 446–450.
503 <https://doi.org/10.1038/ngeo2959>
- 504 Koyaguchi, T., Kaneko, K., 2000. Thermal evolution of silicic magma chambers after basalt
505 replenishments. *Earth and Environmental Science Transactions of The Royal Society of*
506 *Edinburgh* 91, 47–60. <https://doi.org/10.1017/S0263593300007288>
- 507 Li, T., Garg, R., Galvin, J., Pannala, S., 2012. Open-source MFIX-DEM software for gas–solids flows:
508 Part II—Validation studies. *Powder Technology* 220, 138–150.
- 509 Mandeville, C.W., Carey, S., Sigurdsson, H., 1996. Magma mixing, fractional crystallization and volatile
510 degassing during the 1883 eruption of Krakatau volcano, Indonesia. *Journal of Volcanology and*
511 *Geothermal Research* 74, 243–274.
- 512 Martin, V.M., Davidson, J., Morgan, D., Jerram, D.A., 2010. Using the Sr isotope compositions of
513 feldspars and glass to distinguish magma system components and dynamics. *Geology* 38, 539–
514 542. <https://doi.org/10.1130/G30758.1>
- 515 Mastin, L.G., 2002. Insights into volcanic conduit flow from an open-source numerical model.
516 *Geochemistry, Geophysics, Geosystems* 3, 1–18. <https://doi.org/10.1029/2001GC000192>
- 517 McIntire, M.Z., Bergantz George W., Schleicher Jillian M., 2019. On the hydrodynamics of crystal
518 clustering. *Philosophical Transactions of the Royal Society A: Mathematical, Physical and*
519 *Engineering Sciences* 377, 20180015. <https://doi.org/10.1098/rsta.2018.0015>

- 520 Michioka, H., Sumita, 2005. Rayleigh-Taylor instability of a particle packed viscous fluid: Implications
521 for a solidifying magma. *Geophysical Research Letters* 32.
522 <https://doi.org/10.1029/2004GL021827>
- 523 Nakamura, M., 1995. Continuous mixing of crystal mush and replenished magma in the ongoing Unzen
524 eruption. *Geology* 23, 807–810.
- 525 Pallister, J.S., Hoblitt, R.P., Meeker, G.P., Knight, R.J., Siems, D.F., 1996. Magma mixing at Mount
526 Pinatubo: petrographic and chemical evidence from the 1991 deposits. *Fire and mud: eruptions
527 and lahars of Mount Pinatubo, Philippines* 687–731.
- 528 Parmigiani, A., Huber, C., Bachmann, O., 2014. Mush microphysics and the reactivation of crystal-rich
529 magma reservoirs. *Journal of Geophysical Research: Solid Earth* 119, 6308–6322. [https://doi.org/
530 10.1002/2014JB011124](https://doi.org/10.1002/2014JB011124)
- 531 Schleicher, J.M., Bergantz, G.W., 2017. The Mechanics and Temporal Evolution of an Open-system
532 Magmatic Intrusion into a Crystal-rich Magma. *J Petrology* 58, 1059–1072.
533 <https://doi.org/10.1093/petrology/egx045>
- 534 Schleicher, J.M., Bergantz, G.W., Breidenthal, R.E., Burgisser, A., 2016. Time scales of crystal mixing in
535 magma mushes. *Geophysical Research Letters* 43, 1543–1550.
536 <https://doi.org/10.1002/2015GL067372>
- 537 Self, S., 1992. Krakatau revisited: The course of events and interpretation of the 1883 eruption.
538 *GeoJournal* 28, 109–121. <https://doi.org/10.1007/BF00177223>
- 539 Singer, B.S., Costa, F., Herrin, J.S., Hildreth, W., Fierstein, J., 2016. The timing of compositionally-zoned
540 magma reservoirs and mafic ‘priming’ weeks before the 1912 Novarupta-Katmai rhyolite
541 eruption. *Earth and Planetary Science Letters* 451, 125–137.
542 <https://doi.org/10.1016/j.epsl.2016.07.015>
- 543 Snyder, D., Tait, S., 1995. Replenishment of magma chambers: comparison of fluid-mechanic
544 experiments with field relations. *Contrib Mineral Petrol* 122, 230–240.
545 <https://doi.org/10.1007/s004100050123>
- 546 Syamlal, M., 1998. MFIX documentation numerical technique. EG and G Technical Services of West
547 Virginia, Inc., Morgantown, WV (United States).
- 548 Syamlal, M., Rogers, W., OBrien, T.J., 1993. MFIX documentation theory guide. USDOE Morgantown
549 Energy Technology Center, WV (United States).
- 550 Tomiya, A., Takahashi, E., 1995. Reconstruction of an Evolving Magma Chamber beneath Usu Volcano
551 since the 1663 Eruption. *J Petrology* 36, 617–636. <https://doi.org/10.1093/petrology/36.3.617>
- 552 Weinberg, R.F., Leitch, A.M., 1998. Mingling in mafic magma chambers replenished by light felsic
553 inputs: fluid dynamical experiments. *Earth and Planetary Science Letters* 157, 41–56.
554 [https://doi.org/10.1016/S0012-821X\(98\)00025-9](https://doi.org/10.1016/S0012-821X(98)00025-9)
- 555 Wiebe, R.A., 2016. Mafic replenishments into floored silicic magma chambers. *American Mineralogist*
556 101, 297–310. <https://doi.org/10.2138/am-2016-5429>
557
- 558

559

560 Tables:

Symbol (unit)	Definition
d_p (m)	Particle diameter
E (Pa)	Particle Young modulus
\vec{F}_{GPD} (N)	Gravity-Pressure-Drag force
\vec{g} ($m\ s^{-2}$)	Gravity acceleration vector
H_{bed} (m)	Particle bed thickness
H_{max} (m)	Intruded layer maximum height above the inlet
H^*	Dimensionless height of the intruded volume
m_p (kg)	Particle mass
P (Pa)	Fluid pressure
R (m)	Intruder batch radius
t^*	Reduced time
U_{ini} ($m\ s^{-1}$)	Injection superficial velocity
U_{mf} ($m\ s^{-1}$)	Minimum fluidization superficial velocity
U^*	Dimensionless injection velocity
\vec{V}_f ($m\ s^{-1}$)	Fluid velocity vector
\vec{V}_p ($m\ s^{-1}$)	Particle velocity vector
W_{ini} (m)	Injection width
ρ_f ($kg\ m^{-3}$)	Fluid density
η (Pa s)	Fluid dynamic viscosity
τ_v (s)	Particle viscous response time
β ($kg\ s^{-1}$)	Momentum transfer coefficient
Δt (s)	DEM time step
η (Pa s)	Fluid dynamic viscosity
η_i (Pa s)	Intruder melt dynamic viscosity
η_h (Pa s)	Host melt dynamic viscosity
η^*	Melts dynamic viscosity ratio
μ	Particle friction coefficient
ρ_h ($kg\ m^{-3}$)	Host melt density
ρ_i ($kg\ m^{-3}$)	Intruder melt density
ρ_p ($kg\ m^{-3}$)	Average density of the particles
ρ^*	Melts reduced buoyancy
ρ_h^*	Melts bulk reduced buoyancy
σ	Poisson coefficient
τ_v (s)	Particle viscous response time
Φ	Solid volume fraction

561 **Table 1: List of symbols and their meaning**

562

Parameter	Value or range
ρ_p	3300 kg m ⁻³
d_p	4.5-5.5 mm
Nb crystals	208495
H_{bed}	0.3 m
W_{ini}	0.1 m
ρ_i	2500 kg m ⁻³
η_i	1 Pa s
E	2 10 ⁷ Pa
σ	0.32
μ	0.3

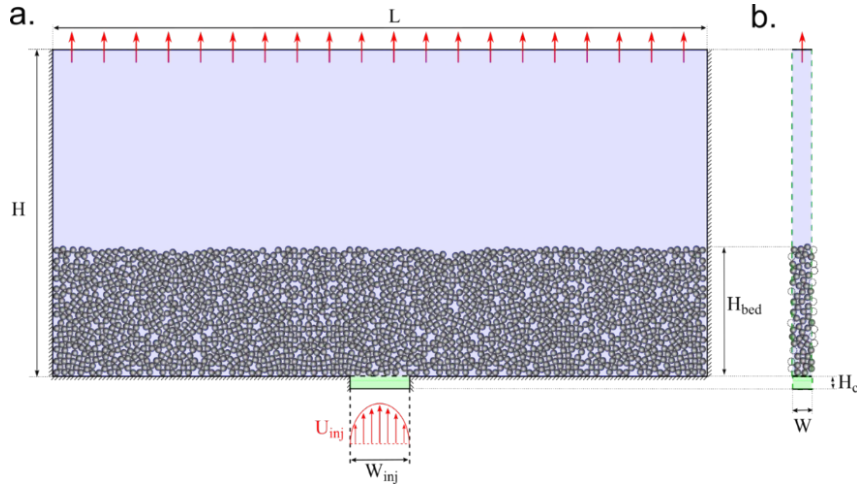
563 **Table 2: Parameters kept constant during the parametric study**

Run nb.	ρ_h (kg m ⁻³)	$\rho_h(host)$ (kg m ⁻³)	ρ^*	ρ_h^*	η_h (Pa s)	U_{mf} (m s ⁻¹)	U_{ini} (m s ⁻¹)
A1	2500	3012	0	-0.2048	1	2.956 10 ⁻⁴	6.268 10 ⁻³
A2	2500	3012	0	-0.2048	5	5.913 10 ⁻⁵	1.254 10 ⁻³
A3	2500	3012	0	-0.2048	10	2.957 10 ⁻⁵	6.268 10 ⁻⁴
A4	2500	3012	0	-0.2048	50	5.913 10 ⁻⁶	1.254 10 ⁻⁴
A5	2500	3012	0	-0.2048	100	2.957 10 ⁻⁶	6.268 10 ⁻⁵
A6	2450	2994	0.02	-0.1976	1	3.141 10 ⁻⁴	6.660 10 ⁻³
A7	2450	2994	0.02	-0.1976	5	6.283 10 ⁻⁵	1.332 10 ⁻³
A8	2450	2994	0.02	-0.1976	10	3.141 10 ⁻⁵	6.660 10 ⁻⁴
A9	2450	2994	0.02	-0.1976	50	6.283 10 ⁻⁶	1.332 10 ⁻⁴
A10	2450	2994	0.02	-0.1976	100	3.141 10 ⁻⁶	6.660 10 ⁻⁵
A11	2550	3030	-0.02	-0.212	1	2.772 10 ⁻⁴	5.876 10 ⁻³
A12	2550	3030	-0.02	-0.212	5	5.544 10 ⁻⁵	1.175 10 ⁻³
A13	2550	3030	-0.02	-0.212	10	2.772 10 ⁻⁵	5.876 10 ⁻⁴
A14	2550	3030	-0.02	-0.212	50	5.544 10 ⁻⁶	1.175 10 ⁻⁴
A15	2550	3030	-0.02	-0.212	100	2.772 10 ⁻⁶	5.876 10 ⁻⁵
A16	2200	2904	0.12	-0.1616	1	4.065 10 ⁻⁴	8.618 10 ⁻³
A17	2200	2904	0.12	-0.1616	5	8.130 10 ⁻⁵	1.724 10 ⁻³
A18	2200	2904	0.12	-0.1616	10	4.065 10 ⁻⁵	8.618 10 ⁻⁴
A19	2200	2904	0.12	-0.1616	50	8.130 10 ⁻⁶	1.724 10 ⁻⁴
A20	2200	2904	0.12	-0.1616	100	4.065 10 ⁻⁶	8.618 10 ⁻⁵
A21	2150	2886	0.14	-0.1544	1	4.250 10 ⁻⁴	9.010 10 ⁻³
A22	2150	2886	0.14	-0.1544	5	8.500 10 ⁻⁴	1.802 10 ⁻³

Run nb.	ρ_h (kg m ⁻³)	ρ_h (<i>host</i>) (kg m ⁻³)	ρ^*	ρ_h^*	η_h (Pa s)	U_{mf} (m s ⁻¹)	U_{ini} (m s ⁻¹)
A23	2150	2886	0.14	-0.1544	10	$4.250 \cdot 10^{-5}$	$9.010 \cdot 10^{-4}$
A24	2150	2886	0.14	-0.1544	50	$8.500 \cdot 10^{-6}$	$1.802 \cdot 10^{-4}$
A25	2150	2886	0.14	-0.1544	100	$4.250 \cdot 10^{-6}$	$9.010 \cdot 10^{-5}$
B1	2150	2886	0.14	-0.1544	100	$4.250 \cdot 10^{-6}$	$4.250 \cdot 10^{-3}$
B2	2150	2886	0.14	-0.1544	100	$4.250 \cdot 10^{-6}$	$4.250 \cdot 10^{-2}$
B3	2150	2886	0.14	-0.1544	100	$4.250 \cdot 10^{-6}$	$4.250 \cdot 10^{-1}$
B4	2150	2886	0.14	-0.1544	100	$4.250 \cdot 10^{-6}$	$4.250 \cdot 10^0$

564 **Table 3: List of the simulation performed for this chapter and corresponding variables.**

565



566

Figure 1: Simulations initial condition. [A] The drawing represents the computational domain

567

viewed from the front. The medium is composed by rectangular box, which is fed by a conduit at

568

its based. Particles are settled to generate a particle bed having a thickness H_{bed} . The background

569

colors indicates which fluid is present initially in the computational domain. The blue color

570

corresponds to the host melt and the green color to the intruded melt. The red arrows below the

571

conduit represent the velocity profile of the injected fluid (Poiseuille flow). The arrows atop the

572

domain indicate that the boundary condition is a fixed pressure outflow. The hatched walls

573

indicate non-slip boundary conditions. [B] Side view of the computational domain. The green

574

dashed lines indicate that cyclical boundary conditions are used for these walls. The dotted circles

575

indicate particles overlapping with one of the two cyclical boundary conditions and that are also

576

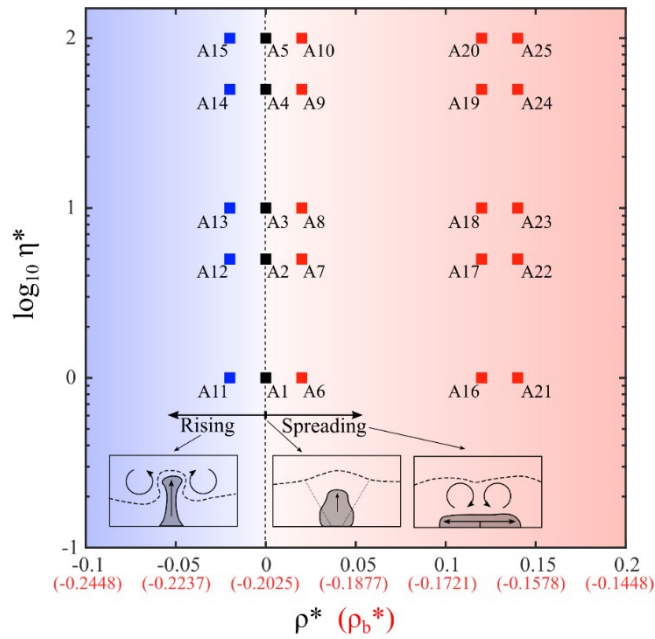
considered to be present on the opposite side.

577

578

579

580

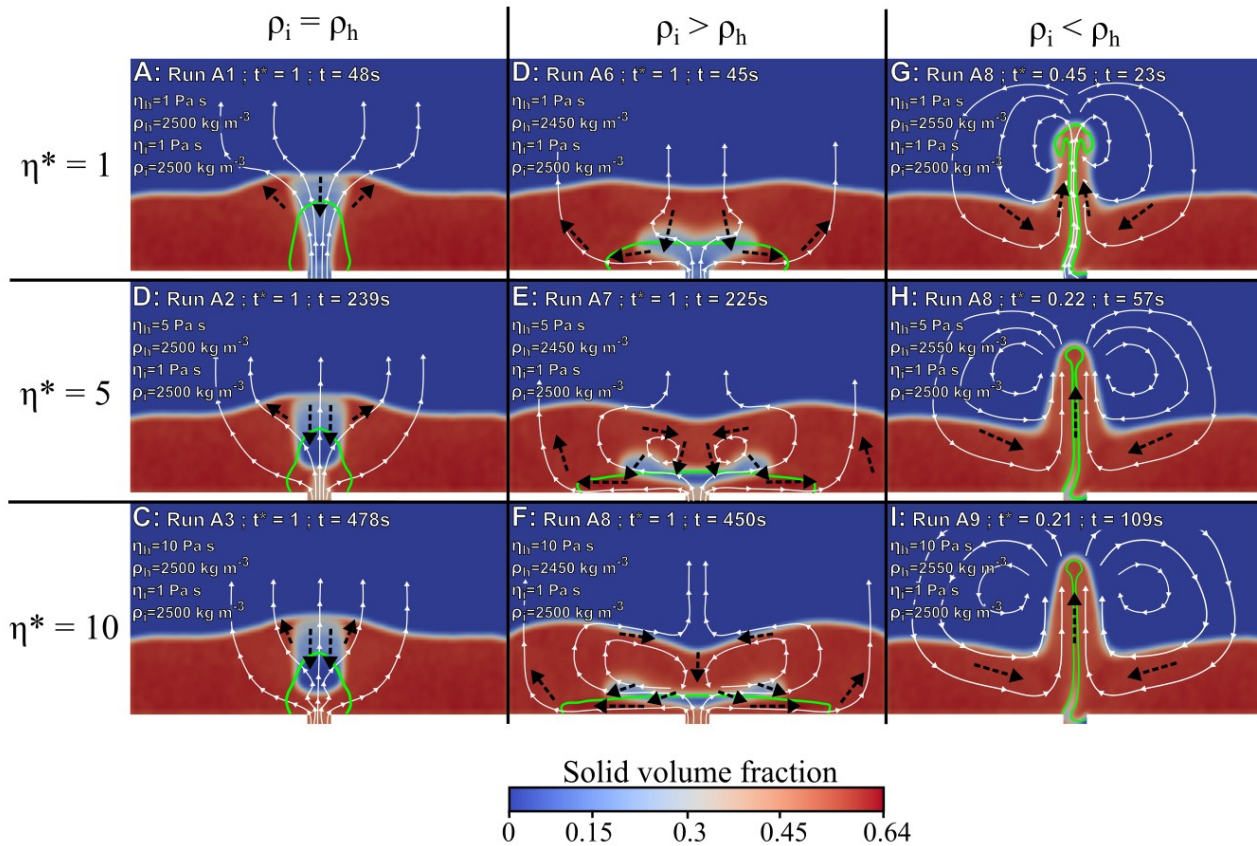


581 **Figure 2:** Regime diagram of intrusion behavior for $U^*=21.2$. The diagram represents the
 582 positions of the simulations A1–25 as functions of the reduced buoyancy (abscissa) and viscosity
 583 ratios (ordinate). Each square represents a simulation. Square colors depend on the observed
 584 regime (blue=rising; black=fluidization; red=lateral spreading). Similarly, the background color
 585 interpolates the observed regimes (blue= rising; red=lateral spreading) and the vertical dashed
 586 line interpolates where the fluidization is expected to prevail.

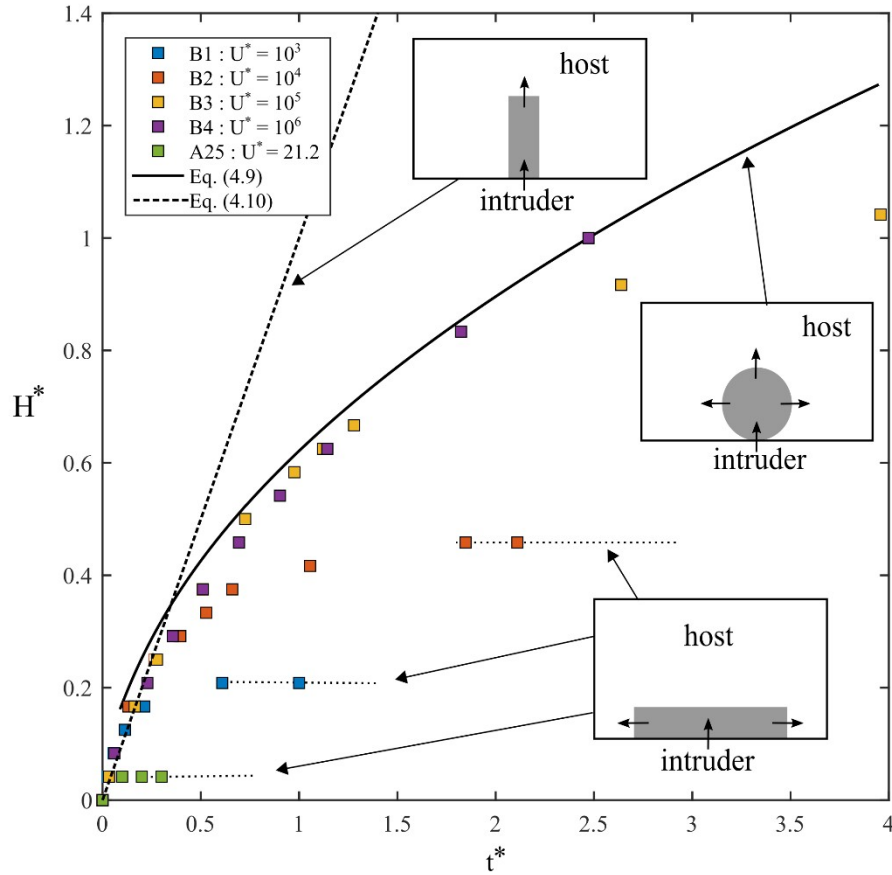
587

588

589

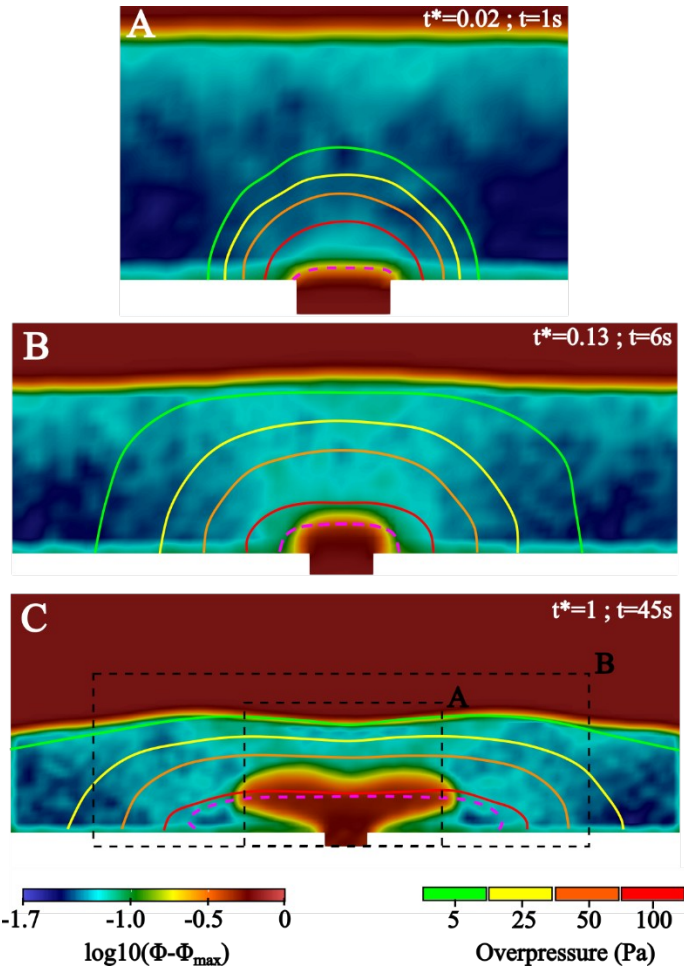


591 **Figure 3:** Comparison of the effects of buoyancy and viscosity contrasts. Each section represents
 592 the advancement of the simulation at $t^*=1$ (or when the rising instability is above the particle
 593 bed). The injected melt contours are indicated with green curves. The dashed black arrows
 594 indicate the presence and direction of granular flows. The thin white curves indicate the fluid
 595 streamlines with small arrowheads indicating flow direction.



598 **Figure 4:** Evolution of the height, H^* , of the intruded volume as a function of the dimensionless
 599 time t^* . Each square represents the height of the top of the intruded volume measured in the
 600 simulations. Square colors indicate injection rate. Dashed lines indicate the theoretical intruder
 601 front height evolution in the case of vertical propagation (supplementary information 3) The
 602 black curve is the theoretical front height for a radial growth, and the horizontal dotted lines

603 indicate the front height evolution during lateral spreading. The three insets illustrate intrusion
 604 behaviors.

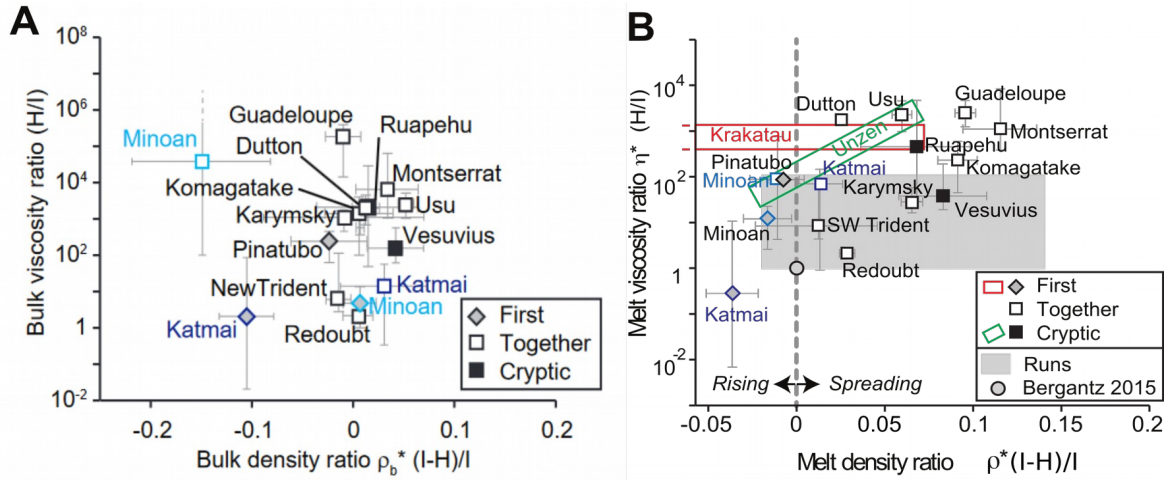


605

606 **Figure 5:** Evolution of the pore pressure and crystal volume fraction. On each inset, the color
 607 depend on the difference between the local crystal volume fraction, Φ , and the maximum one,
 608 Φ_{max} ($\Phi_{max}=0.64$), in a logarithmic scale. The overpressure respect to the initial hydrostatic
 609 pressure field is indicated with contour that corresponds to the isosurfaces where the overpressure
 610 are equal to 5, 25, 50, and 100 Pa. The pink dashed curves represent the boundary between the

611 injected and resident melt. Inset [A] and [B] are captured after 1s and 6s. Both only displayed the
612 portion of the mush layer that present overpressure and dilation. Inset [C] is acquired after 45s
613 and cover a slice of the entire computational domain. The two dashed rectangle indicate the
614 extend of insets [A] and [B].

615



616

617 **Figure 6:** [A] Ratios of bulk properties for the host and intruder magmas involved in 15
 618 eruptions. The bulk viscosity ratio is that of the host over that of the intruder and the bulk density
 619 ratio is that of the difference between the intruder and the host over that of the intruder. Eruptions
 620 are sorted according to whether the intruder magma was erupted first (“First”), at the same time
 621 as (or mixed with) the host (“Together”), or fully mixed with the host (“Cryptic”). [B] Ratios of
 622 melt properties for the host and intruder magmas involved in 15 eruptions. The melt viscosity
 623 ratio is that of the host over that of the intruder and the melt density ratio is that of the difference
 624 between the intruder and the host over that of the intruder. Eruptions are sorted according to
 625 whether the intruder magma was erupted first (“First”), at the same time as (or mixed with) the
 626 host (“Together”), or fully mixed with the host (“Cryptic”). The gray area covers the runs done in
 627 this study and the cross marks the parameters used in the numerical study of Bergantz et al.
 628 (2015). See text for details regarding the special cases of Unzen and Krakatau.

629

630

631

632 **Supplementary Information 1:**

 633 This Supplementary Information includes two tables summarizing the equation system
 634 solved in our numerical simulations (Tables S1-S2).

 635 **Table S1:** List of the equations implemented in the CFD-DEM model

Equation names	Equations	Ref.
Mass conservation	$\frac{\partial \varepsilon_f}{\partial t} + \nabla \cdot (\varepsilon_f \vec{v}_f) = 0$	1
Momentum conservation	$\rho_f \left(\frac{\partial}{\partial t} (\varepsilon_f \vec{v}_f) + \nabla \cdot (\varepsilon_f \vec{v}_f \otimes \vec{v}_f) \right) = \nabla \cdot (\sigma'_f) + \varepsilon_f \rho_f \vec{g} + \vec{I}_f$	1
Stress tensor	$\sigma'_f = P_f \delta_{ij} + \frac{2}{3} \eta_f \text{tr}(\dot{\epsilon}_f) \delta_{ij} + 2 \eta_f \dot{\epsilon}_f$	1
Euler velocity integration	$\vec{v}_p^{(k)}(t + \Delta t) = \vec{v}_p^{(k)}(t) + \Delta t \frac{\vec{F}_{GPD}^{(k)}(t) + \sum_{l=1}^{N_f^k} (\vec{F}_C^{N(k,l)}(t) + \vec{F}_C^{T(k,l)}(t))}{m^{(k)}}$	Eq. (4.4)
Euler displacement integration	$\vec{X}_p^{(k)}(t + \Delta t) = \vec{X}_p^{(k)}(t) + \Delta t \vec{v}_p^{(k)}(t + \Delta t)$	2
Euler rotation integration	$\vec{\omega}_p^{(k)}(t + \Delta t) = \vec{\omega}_p^{(k)}(t) + \Delta t \frac{\sum_{l=1}^{N_f^k} (\vec{T}_C^{(k,l)} + \vec{T}_L^{(k,l)}(t))}{I^{(k)}}$	2
Normal contact force	$\vec{F}_c^{N(i,j)}(t) = \left(-k_n^{(i,j)}(t) \delta_n^{(i,j)}(t) + \eta_n^{(i,j)}(t) \Delta \vec{V}_p^{N(i,j)}(t) \right) \vec{n}_{ij}$	2 5
Tangential contact force	$\vec{F}_c^{T(i,j)}(t) = -k_t^{(i,j)}(t) \delta_t^{(i,j)}(t) + \eta_t^{(i,j)}(t) \Delta \vec{V}_p^{T(i,j)}(t)$	2 5
Collisional torque	$\vec{T}_c^{(i,j)}(t) = \frac{d_p^{(i)} - \delta_n^{(i,j)}(t)}{2} \vec{F}_c^{T(i,j)}(t); \vec{T}_c^{(j,i)}(t) = \frac{d_p^{(j)} - \delta_n^{(i,j)}(t)}{2} \vec{F}_c^{T(i,j)}(t)$	2
normal spring (Hertzian model)	$k_n^{(i,j)}(t) = \frac{4}{3} \frac{E^{(i)} E^{(j)} \sqrt{R_{eff}^{(i,j)}}}{E^{(j)} (1 - \sigma^{(j)2}) + E^{(i)} (1 - \sigma^{(i)2})} \delta_n^{(i,j) \frac{1}{2}}(t)$	2
tangential spring (Hertzian model)	$k_t^{(i,j)}(t) = \frac{16}{3} \frac{G^{(i)} G^{(j)} \sqrt{R_{eff}^{(i,j)}}}{G^{(j)} (2 - \sigma^{(i)}) + G^{(i)} (2 - \sigma^{(j)})} \delta_t^{(i,j) \frac{1}{2}}(t)$	2

Equation names	Equations	Ref.
Elastic modulus	$G = \frac{E}{2(1+\sigma)}$	2
Normal damping coefficient	$\eta_n^{(i,j)}(t) = \frac{2\sqrt{m_{eff}^{(i,j)} k_n^{(i,j)}(t)} \ln e_n }{\sqrt{\pi^2 + \ln^2 e_n}} \delta_n^{(i,j)}(t)^{\frac{1}{4}}$	2 5
Tangential damping coefficient	$\eta_t^{(i,j)} = \frac{2\sqrt{m_{eff}^{(i,j)} k_t^{(i,j)}(t)} \ln e_t }{\sqrt{\pi^2 + \ln^2 e_t}} \delta_t^{(i,j)}(t)^{\frac{1}{4}}$	2 5
effective radius	$R_{eff}^{(i,j)} = \frac{2(d p^{(i)} + d_p^{(j)})}{d_p^{(i)} d_p^{(j)}}$	2
Effective mass	$m_{eff}^{(i,j)} = \frac{m^{(i)} + m^{(j)}}{m^{(i)} m^{(j)}}$	2
Solids/Fluid momentum exchange on REV	$\vec{I}_f(t) = \frac{1}{V_{REV}} \sum_{k=1}^{N_k} \vec{F}_D^{(k)}(t) K_{REV}(X_p^{(k)})$	2
Drag forces (for the fluid)	$\vec{F}_D^{(k)}(t) = -\nabla P_f(t) \left(\frac{\pi}{6} d_p^{(k)3} \right) + \frac{\beta_{fs}^{(k)}(t)}{(1-\varepsilon_f(t))} \left(\frac{\pi}{6} d_p^{(k)3} \right) (\vec{v}_f(t) - \vec{v}_p^{(k)}(t))$	2
Local fluid/solid momentum transfer	$\beta_{fs}^{(k)}(t) = \begin{cases} \frac{3}{4} C_D^{(k)}(t) \frac{\rho_f \varepsilon_f(t) (1-\varepsilon_f) \ \vec{v}_f - \vec{v}_s^{(k)}\ }{d_p^{(k)}} \varepsilon_f^{-2.65} & \varepsilon_f \geq 0.8 \\ \frac{150(1-\varepsilon_f(t))^2 \eta_f + 1.75 \rho_f (1-\varepsilon_f(t)) \ \vec{v}_f(t) - \vec{v}_s^{(k)}(t)\ }{\varepsilon_f(t) d_p^{(k)2} + d_p^{(k)}} \varepsilon_f & \end{cases}$	3 4
Drag coefficient	$C_D^{(k)}(t) = \begin{cases} \frac{24}{Re^{(k)}(t) (1+0.15 Re^{(k)}(t)^{0.687})} & Re^{(k)}(t) < 1000 \\ 0.44 & Re^{(k)}(t) \geq 1000 \end{cases}$	3 4
Particle Gravity-Drag-Pressure force	$\vec{F}_{GPD}(t) = \frac{m_p}{\Delta t} \left(\vec{v}_f + \tau_v \left(\vec{g} - \frac{\nabla P}{\rho_p} \right) - \vec{v}_p(t) \right) \left(1 - e^{-\frac{\Delta t}{\tau_v}} \right)$	Eq. (4.5)
Reynolds number	$Re^{(k)}(t) = \frac{d_m^{(k)} \ \vec{v}_f(t) - \vec{v}_s^{(k)}(t)\ \rho_f}{\eta_f}$	3

637 ² Garg et al., (2010)

638 ³ Benyahia et al., (2012)

639 ⁴ Gidaspow, (1986)

640

641 **Table S2 : Symbols used in Table S1**

Symbol	Definition
$C_D^{(k)}$	Drag coefficient of the k th particle
$d_p^{(i)}$	i th particle diameter
e_n	Particle normal restitution coefficient
e_t	Particle tangential restitution coefficient
$E^{(i)}$	i th particle Young modulus
$\vec{F}_C^{N(k,l)}$	Normal contact force between k th particle and its l th neighbor
$\vec{F}_C^{T(k,l)}$	Tangential contact forces between k th particle and its l th neighbor
$\vec{F}_D^{(k)}$	Drag force on k th particle
\vec{g}	Gravitational vector (m s ⁻²)
$G^{(k)}$	k th particle shear moduli
$h^{(i,j)}$	Distance between i th and j th particles edges
\vec{I}_f	Fluid-solid momentum exchange
$I^{(k)}$	k th particle moment of inertia
K_{REM}	Generic kernel to determine the influence of a particle located at $\vec{X}_p^{(k)}$ on the REV
$k_n^{(i,j)}$	Normal spring coefficient between i th and j th particles contact
$k_t^{(i,j)}$	Tangential spring coefficient between i th and j th particles contact
l	Neighbors index
$m^{(k)}$	k th particle mass
$m_{eff}^{(i,j)}$	i th and j th particles effective radius

$N_l^{(k)}$	Number of neighbors of the k^{th} particle
N_k	Number of particles
\vec{n}_{ij}	Normal vector between i^{th} and j^{th} particles
P_f	Fluid pressure (Pa)
REV	Representative elementary volume
$Re^{(k)}$	i^{th} particle Reynolds number
$R_{eff}^{(i,j)}$	i^{th} and j^{th} particles effective radius
$R_{\square}^{(i,j)}$	Contact area radius between i^{th} and j^{th} particles
$\vec{T}_C^{(k,l)}$	Contact torque between k^{th} particle and its l^{th} neighbor
$\vec{T}_L^{(k,l)}$	Lubrication torque between k^{th} particle and its l^{th} neighbor
\vec{v}_f	Fluid velocity vector (m s^{-1})
$\vec{v}_p^{(k)}$	k^{th} particle velocity vector (m s^{-1})
$\vec{X}_p^{(k)}$	k^{th} particle position (m)
$\beta_{fs}^{(k)}$	k^{th} particle - fluid momentum transfer coefficient
$\Delta V_p^{N(i,j)}$	Normal relative velocity between i^{th} and j^{th} particles
$\Delta V_p^{T(i,j)}$	Tangential relative velocity between i^{th} and j^{th} particles
δ_{ij}	Kronecker tensor
$\delta_n^{(i,j)}$	Normal overlap between i^{th} and j^{th} particles
$\delta_t^{(i,j)}$	Tangential displacement during the contact between i^{th} and j^{th} particles contact
ε	Roughness distance below which lubrication is ineffective (m)
ε_f	Fluid volume fraction
$\dot{\varepsilon}_f$	Fluid strain rate tensor
η_f	Fluid viscosity (Pa s)
$\eta_n^{(i,j)}$	Normal damping coefficient between i^{th} and j^{th} particles
$\eta_t^{(i,j)}$	Tangential damping coefficient between i^{th} and j^{th} particles

V	Domain volume (m^3)
ρ_f	Fluid density (kg m^{-3})
$\sigma^{(i)}$	i^{th} particle Poisson coefficient
σ'_f	Fluid stress tensor
$\vec{\omega}_p^{(k)}$	k^{th} particle rotation vector (rad s^{-1})
∇	Nabla operator
\otimes	Outer product

642

643

644 **Supplementary Information 2:**

645 This supplementary information presents an updated derivation of the minimum
646 fluidization velocity compared to those used in the literature.

647 The onset of fluidization of a crystal bed occurs when the upward drag force exerted by
648 the injected fluid exceed its net weight. Shi et al. (1984) proposed a formula to predict the
649 minimum fluidization velocity of a random packed bed due to a localized injection of fluid. These
650 authors made the assumption that the fluid velocity is only vertical and uniformly distributed on
651 horizontal cross-sectional area (Fig. S1). The total upward drag force is computed with the
652 Ergun's formula (Ergun, 1952) for a bed fluidized uniformly. Later, Cui et al. (2014) adapted this
653 formula by considering the fluid velocity uniform along a semi-circular cross sectional area.
654 Here, we modify the approach of Cui et al. (2014) to predict the minimum fluidization velocity in
655 the experimental apparatus geometry because the original derivation incorrectly assumed the
656 distance between the injection point and center of the inlet, r_0 , and the boundaries of the
657 integral in their Eq. (13).

658 The total upward drag force applied by the inlet on the particle bed is computed as:

$$659 \quad F_D = \int_{r_0}^{H+r_0} (AU_r + BU_r^2) S(r) dr, \quad (S1)$$

660 where r_0 correspond of the vertical coordinates of the bottom and $H+r_0$ is the position of the
 661 top of the particle bed. The variable r corresponds to the radial distance from a hypothetic
 662 injection point (Fig. S1). A and B are given by Ergun (1952):

$$663 \quad A = 150 \frac{\phi^2}{(1-\phi)^3} \frac{\eta_f}{d_p^2}, \quad (S2)$$

$$664 \quad B = 1.75 \frac{\phi}{(1-\phi)^3} \frac{\rho_f}{d_p}. \quad (S3)$$

665 $S(r)$ represents the area of the curved surface on which the fluid velocity is uniform, and it is
 666 computed as a function of r as:

$$667 \quad S(r) = 2\alpha(r+r_0)W_l. \quad (S4)$$

668 U_r is the fluid velocity at a radial distance r . U_r may be computed by considering that the
 669 injected flux is conserved through the particle bed height, which yields:

$$670 \quad Q_{inj} = U_r S(r), \quad (S5)$$

671 and, with (S4):

$$672 \quad U_r = \frac{Q_{inj}}{2\alpha(r+r_0)W_l} \quad (S6)$$

673 Substituting Eqs. (S6) and (S4) into Eq. (S1) yields:

$$674 \quad F = A Q_{inj} H_0 + \frac{B Q_{inj}^2}{2\alpha W_l} \ln \left(\frac{H_0 + 2r_0}{2r_0} \right) \quad (S7)$$

675 In this geometry, the net weight of the bed, W , is given by:

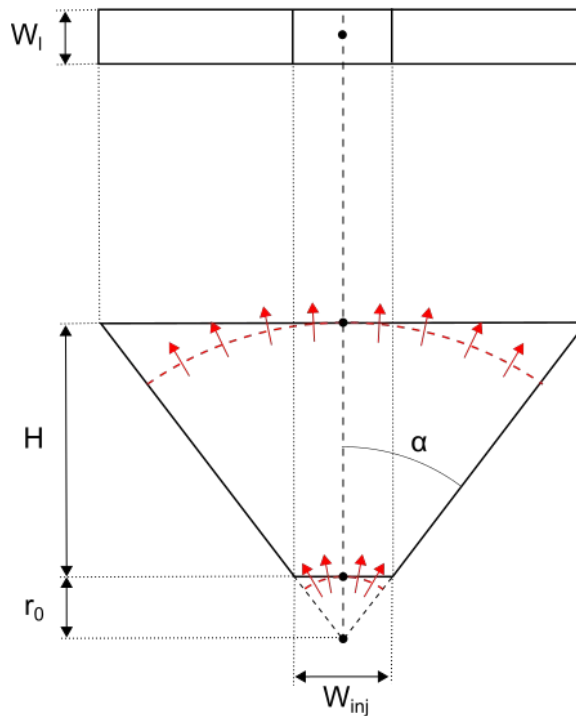
$$676 \quad W = \left[(r_0 + H_0)^2 \tan \alpha - \frac{W_{inj} r_0}{2} \right] W_l (\rho_p - \rho_f) g \phi. \quad (S8)$$

677 Introducing $r_0 = W_{inj} / (2 \tan \alpha)$, the onset of fluidization occurred when $F = W$, which yields:

$$678 \quad A Q_{inj} H_0 + \frac{B Q_{inj}^2}{2 \alpha W_l} \ln \left(\frac{2 \tan \alpha}{W_{inj}} + 1 \right) - [H_0 (W_{inj} + H_0 \tan \alpha)] W_l (\rho_p - \rho_f) g \phi = 0 \quad (S9)$$

679 Figure S2 displays comparison of the minimum fluidization velocities computed with
 680 formulas from Ergun (1952), Shi et al. (1984), Cui et al., (2014), and Eq. (S9), function of the
 681 particle bed height. It shows that Eq (S9) is closer to the result predicted with the formulas from
 682 Ergun (1952) and Shi et al. (1984). The incorrect formula derived by Cui et al., (2014) results in
 683 the significant overestimations of the minimum fluidization velocity.

684



685 **Figure S1:** Conceptual framework to derive the minimum fluidization velocity. The top draw is a
 686 view from the top. The bottom draw is a front view. On both draws, the thick black lines
 687 represent the boundaries of the volume of the particle bed, which is fluidized. The red dashed
 688 curves indicate the cross sectional areas where the magnitude of the fluid velocity is uniform.
 689 The arrows represent the direction of the fluid flow. The black dots represent the positions of
 690 the theoretical injections point and intersections between the cross sectional areas where the
 691 fluid velocity is uniform and the vertical boundary of the fluidized particle bed.

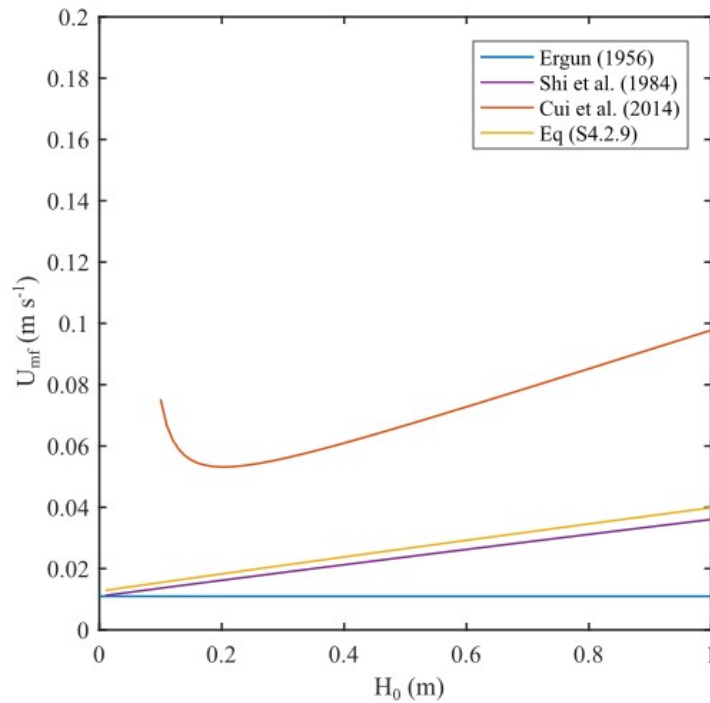
692

693

694

695

696



697 **Figure S2:** Comparison of the minimum fluidization velocities function of the initial particle bed
698 height. The curves represent the minimum fluidization velocities derived by authors and the one
699 given here.

700

701

702 **Supplementary Information 3:**

703 This supplementary information presents the derivation of the maximum height of the
704 intrusion as a function of the time for end member scenarios.

705 We consider two end-members for the growth of the intrusion volume (vertical or
706 radial). The first end member considers the vertical ascent (dyking) of the intruded melt above
707 the inlet over a width, W_{inj} . In this case, the ratio, H^* , between H_{max} and the initial particle bed
708 thickness, H_{bed} ($H^* = H_{max} / H_{bed}$), reads:

709
$$H^* = t^*. \tag{S10}$$

710 In the case of radial growth, we consider as spherical intrusion having a unknown radius,
711 R , and fed by an inlet of width W_{inj} (Fig. S3). The inlet truncates the sphere at a vertical distance,
712 h , which depends on both R and W_{inj} . The objective is to compute the distance from the inlet to
713 the top of the sphere, H , knowing the area A and injection width W_{inj} . The total area, A_{tot} , of
714 the sphere is the sum of the area A , where the intruded fluid is present and the truncated area
715 B as:

716
$$A_{tot} = A + B. \tag{S11}$$

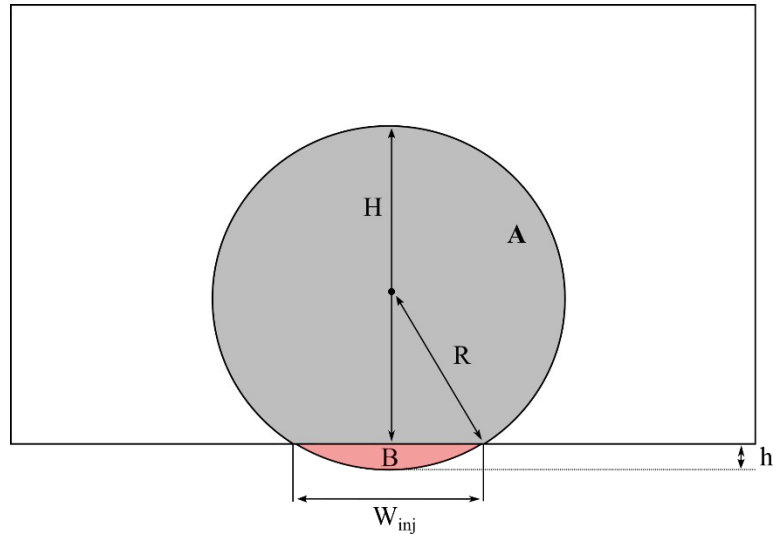
717 The area A depends on injection velocity and time. The area A_{tot} may be expressed using the
718 sphere radius R . Replacing A and A_{tot} in equation (S11) and rearranging yields:

719
$$\pi R^2 = W_{inj} H_{bed} t^* + A_B. \tag{S12}$$

720 The area B may be approximated with a good accuracy as (Harris and Stöcker, 1998, pp 92-93):

721
$$A_B \approx \frac{2}{3} W_{inj} h + \frac{h^3}{2 W_{inj}}. \tag{S13}$$

722 Inserting Eq. (S13) in Eq. (S12) gives:



723
$$0 = W_{inj} H_{bed} t^* + \frac{2}{3} W_{inj} h + \frac{h^3}{2W_{inj}} - \pi R^2. \quad (S14)$$

724 Equation (S14) contains two unknowns, R and h , which can be related to each other tanks to
 725 geometry:

726
$$0 = \frac{W_{inj}^2}{4} + (R - h)^2 - R^2. \quad (S15)$$

727 Using that $H = 2R - h$, H_{max} may be computed as a function of t^* by solving Equations (S14–S15).

728

729

730

731

732

733

734

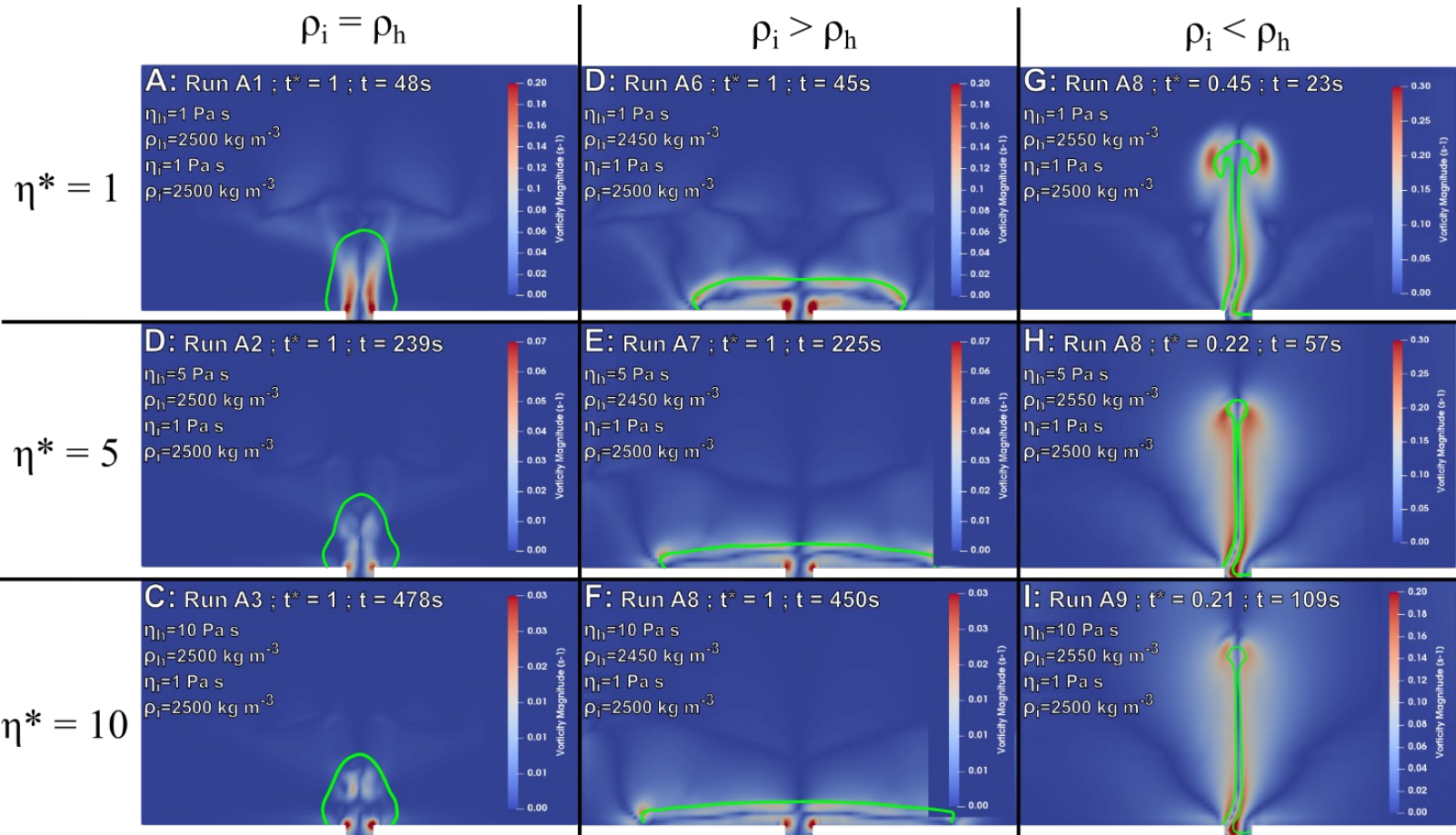
735 **Figure S3:** Schematics of the geometrical setup. The drawing represents a section
736 perpendicular to the intrusion. The area covered by the injected melt is in gray and the area

737

Supplementary information 4:

738

This supplementary figures displays the magnitude of the vorticity.



739 **Figure S4:** Magnitude of the vorticity. Simulations correspond to the ones represented in Fig.
740 3 for the same time steps. The green curves indicate the injected melt contour.

741 **Supplementary information 5:**

742

743 This supplementary section present the physical properties of the end members materials
744 involved in the 15 eruption considered in this study. In cases where mixing was so preeminent that
745 only mixed products were erupted (e.g., Unzen), pre-mixing host characteristics, including crystal
746 content, were determined using indirect evidences such as crystal rims in disequilibrium with the
747 surrounding melt. Viscosities and densities of intruder magmas were sometimes directly
748 characterized because they were erupted (e.g., Pinatubo; Pallister et al., 1996) or approximated using
749 petrological inferences (e.g., Usu, where the melt SiO₂ content was estimated by Tomiya and
750 Takahashi, 1995, from mixing lines and end-members). The software Conflow (Mastin, 2002) was
751 used to calculate densities and viscosities when necessary.

752 All host magmas are mushes except one simple case and three complex cases. The Usu
753 reservoir contained a nearly aphyric (2–5 vol.% crystals) rhyolite prior to the 1663 eruption (Tomiya
754 and Takahashi, 1995). We left this straightforward case in our analysis for completeness; removing it
755 would not affect our results. We treated the next three complex cases separately in our analysis.
756 Krakatau is a compositionally zoned reservoir with a gradient in crystal content ranging from 4–15
757 vol.% in the felsic (dacitic to rhyodacitic) parts of the reservoir to aphyric in the more mafic (andesite)
758 parts of the reservoir (Mandeville et al., 1996). The second case is the Bronze Age eruption of
759 Santorini volcano known as the Minoan eruption. In one scenario, the reservoir that hosted the
760 Minoan eruption products had 10–20 vol% crystals (Cadoux et al., 2014). In others, more complex
761 scenarios have been proposed (Druitt, 2014; Flaherty et al., 2018; Martin et al., 2010). In one, the
762 main rhyodacite would have instead acted as the intruder into an adjacent mushy, mafic reservoir

763 (Druitt, 2014). We reported these two possibilities. The 1912 eruption at Katmai–Novarupta is also a
764 case where the roles of the intruder and host might be reversed (e.g. Coombs and Gardner, 2001;
765 Eichelberger and Izbekov, 2000; Hammer et al., 2002; Singer et al., 2016). We reported the scenario
766 in which the most crystal-rich components (andesite and dacite) are the hosts and the nearly aphyric
767 rhyolite is the intruder (Eichelberger and Izbekov, 2000), as well as the scenario in which the host is
768 composed of a zoned chamber and the intruder is a basaltic andesite (Singer et al., 2016).

769 There is a last complex case that is analyzed individually although its reservoir unambiguously
770 contained a mush. Two mutually exclusive intrusion scenarios have indeed been proposed to explain
771 the 1991–1995 eruption of Unzen volcano. In both scenarios, the host magma was a phenocryst-rich,
772 low-temperature rhyolite mush and the intruder was a nearly aphyric, high-temperature magma
773 (Holtz et al., 2004; Nakamura, 1995). The composition of the intruder, which left only cryptic
774 indications of its presence such as reverse zoning of the outer rims of hornblende, plagioclase and
775 magnetite (Nakamura, 1995), could have been either andesitic (Holtz et al., 2004), or basaltic
776 (Browne et al., 2006).

777

778

779 **Table S3:** Host properties from natural cases (volcano names are followed by the starting year of the eruption). Minerals abbreviations are plagioclase
 780 (Plag), clinopyroxene (CPx), orthopyroxene (OPx), pyroxene (Px), and hornblende (Hb). Only the main mineral phases were taken into account and numbers
 781 in parenthesis are mineral volume proportions. Bulk densities were calculated with a plagioclase density of 2570 kg/m³ and a density of 3200 kg/m³ for all
 782 other minerals. Bulk viscosities were calculated as $\eta_l (1 - \varphi/0.6)^{-2.5 \cdot 0.6}$, where η_l is melt viscosity and φ is crystal volume fraction, except for the Minoan
 783 scenario 2 where the largest bul viscosity was capped at 10¹⁰ Pa s because the higher bound of φ is >0.6. Abbreviations sat. and usat. mean saturated and
 784 undersaturated, respectively. Not used (n.u.) implies that melt densities and/or viscosities were directly given in the reference(s) corresponding to that
 785 case.

786

CASE	Name	Xtal (vol%)	Minerals	Melt SiO ₂ (wt%)	Melt H ₂ O (wt%)	Melt density (kg/m ³)	Melt viscosity (Pa s)	T (°C)	P (MPa)	Ref
Unzen 1991	Dacite	34-35	Plag (0.8) Cpx (0.2)	75	8	2229-2239	1.3×10 ⁴ -1.4×10 ⁴	775	300	1
Vesuvius -79	White Pumice	31.6-40	Plag	53-57	sat.	2218-2300	2.4×10 ³ -3.0×10 ³	875-900	150 ^b	2
Guadeloupe 1530	Andesite	48.3-57.5	Plag (0.8) Px (0.2)	73-75	5.5-6	2189-2203	1.2×10 ⁴ -2.5×10 ⁴	825-875	135-200	3
Karymsky 1996	Andesite	25-32	Plag (0.8) Px (0.2)	63	sat.	2395-2378 ^a	8.9×10 ³ -13×10 ³ ^a	1023-1057	200 ^b	4
Ruapehu 1995	Andesite	24.5-42	Plag (0.66) Px (0.33)	62-70	1-1.5	2380-2438	2.9×10 ⁴ -4.7×10 ⁴	920-1030	40	5
Katmai 1912 – scenario 1	Andesite	30-45	Plag (0.8) Px (0.2)	67.6-74	usat-sat.	2274-2284	1.2×10 ⁴ -1.3×10 ⁴	920-970	75-120	6
	Dacite	30-45	Plag (0.8) Px (0.2)	79.1	usat-sat.	2189-2220	2.0×10 ⁵ -8.1×10 ⁵	850-910	60-25	
Katmai 1912 – scenario 2	Andesite	30	Plag (0.8) Px (0.2)	67.6	usat.	2274	1.2×10 ⁴	920	75	7
	Rhyolite	2	Plag	77	4	2225	1.7×10 ⁶	790	40	
Komagatake 1640	White Pumice	25-43.1	n.u.	74.7-76.1	3-4	2280-2300	4.4×10 ⁴ -2.9×10 ⁵ ^a	970-980	n.u.	8

Montserrat 1995	Andesite	35-45	Plag	75-80	4.8	2171-2160	3.7×10^4 - 8.4×10^4	835-880	105-155	9
Redoubt 1990	Dacite	24-32	Plag	78.5-81	4	2164-2174	3.4×10^4 - 3.8×10^4	840-950	100	10
Krakatau 1883	White Rhyodacite	7-15	Plag	70-74	4	2220-2400	3.1×10^4 - 3.4×10^4	880-890	100-150	11
	Gray Dacite	4-12	Plag	66.5-75	4	2190-2200	1.3×10^4 - 1.4×10^4	890-913	100-150	
Minoan - scenario 1	Rhyodacite	10-20	Plag	73.5-74	5-6	2222-2173	1.7×10^4 - 1.4×10^5	845-860	200-250	12
Minoan - scenario 2	Andesite	55-100	Plag (0.8) CPx (0.2)	71-77	sat. ^b	2213-2231	5.9×10^5 - 1.3×10^7	700-820	50	13
SW Trident 1953	Dacite	37-39	Plag (0.8) Px (0.2)	75	3.6	2190-2200	4.5×10^4 - 4.9×10^4	890	90	14
Dutton 1989	Dacite	35	Plag (0.8) OPx (0.2)	78	sat.	2481-2491	1.4×10^5 - 1.5×10^5	865	200 ^b	15
Pinatubo 1991	White Pumice	47	Plag (0.8) Hb (0.2)	76	6-6.5	2166	5.4×10^4	750-800	155-200	16
	Tan Pumice	15-26	Plag (0.8) Hb (0.2)	73	6-6.5	2194	5.6×10^4	750-800	155-200	
Usu 1663	Silicic magma	2.6-5.3	Plag (0.8) OPx (0.2)	74	n.u.	2210-2224	9.5×10^4 - 2.6×10^5	750-800	n.u.	17

787 ^a Calculated from bulk values given in the reference(s).

788 ^b Assumed value.

789 ^c References are: 1) Holtz et al. (2005), Vetere et al. (2008)(andesite intruder), Browne et al. (2006)(basalt intruder); 2) Cioni et al. (1995), Scaillet et al. (2008); 3) Pichavant
790 et al. (2018); 4) Izbekov et al. (2002), Izbekov et al. (2004), Eichelberger and Izbekov (2000); 5) Nakagawa et al. (1999), Nakagawa et al. (2002), Kilgour et al. (2013); 6)
791 Eichelberger and Izbekov (2000), Coombs and Gardner (2001); 7) Hammer et al. (2002), Singer et al. (2016); 8) Takahashi and Nakagawa (2013); 9) Barclay et al. (1998),
792 Murphy et al. (2000), Couch et al. (2001), Humphreys et al. (2010), Plail et al. (2018); 10) Wolf and Eichelbeger (1997), Nye et al. (1994), Swanson et al. (1994); 11) Camus et
793 al. (1987), Self (1992), Mandeville et al. (1996); 12) Cottrell et al. (1999), Druitt et al. (1999), Cadoux et al. (2014), Flaherty et al. (2018); 13) Druitt (2014); 14) Coombs et al.
794 (2000), Coombs et al. (2002); 15) Miller et al. (1999); 16) Pallister et al. (1992), Pallister et al. (1996), Bernard et al. (1996); 17) Tomiya and Takahashi (2005).

795 **Table S4:** Intruder properties from natural cases. Minerals abbreviations are plagioclase (Plag), clinopyroxene (CPx), pyroxene (Px), hornblende (Hb), olivine
 796 (Ol), and Augite (Aug). Abbreviations and references are the same as in Table S1.

CASE	Name	Xtal (vol%)	Minerals	Melt SiO ₂ (wt%)	Melt H ₂ O (wt%)	Melt density (kg/m ³)	Melt viscosity (Pa s)	T (°C)	P (MPa)
Unzen 1991	Andesite	0-10	Plag ^b	62-64	4	2184-2194	3.2×10 ² -3.2×10 ²	1030-1130	300
	Basalt	0-5	Ol	50	sat. ^b	2351-2418	2.3-10	1030-1200 ^b	300 ^b
Vesuvius -79	K-rich basalt	0-20	Plag	50-52	usat.	2485-2441	13-16	1050-1140	150 ^b
Guadeloupe 1530	Basalt	0-12	Plag	50-53	5-6	2436-2420	5.4-9.3	975-1025	200 ^b
Karymsky 1996	Basalt	20	Plag	52	sat.	2545 ^a	22-54	1080-1115	200 ^b
Ruapehu 1995	High-T magma	0-10	Plag ^b	54.2-57.7	1-1.5	2530-2640	10-10 ²	1100 ^b -1200 ^b	40
Katmai 1912 – scenario 1	Rhyolite	2	Plag	77	4	2225-2172	7.5×10 ³ -1.7×10 ⁶	790-850	40-100
Katmai 1912 – scenario 2	Andesite	30-45	Plag (0.8) Px (0.2)	67.6-74	usat.-sat.	2274-2284	1.2×10 ⁴ -1.3×10 ⁴	920-970	75-120
Komagatake 1640	Basalt	0		57	n.u.	2500 ^b -2540	5.0×10 ³ -1.0×10 ^{3 a}	1150	n.u.
Montserrat 1995	Mafic recharge	2-4.5	Plag	52-71	sat.	2400-2500	10-10 ²	975-1196	105-155
Redoubt 1990	Andesite	24-32	Plag	64.5-66	4	2228-2238	1.6×10 ⁴ -1.8×10 ⁴	840-950	100
Krakatau 1883	Basalt	0-10 ^b	Plag ^b	61.6	sat. ^b	2355-2363	24-31	984-1011	100-150
Minoan – scenario 1	Mafic	22-40	Plag (0.8) CPx (0.2)	61-63	sat. ^b	2157-2167	6.1×10 ³ -6.7×10 ³	880	50
Minoan – scenario 2	Rhyodacite	10-20	Plag	73.5-74	5-6	2213-2173	1.7×10 ⁴ -1.4×10 ⁵	845-860	200-250

Non-peer reviewed preprint submitted to EarthArXiv

SW Trident 1953	Andesite	28-43	Plag	74-63	3.5	2150-2295	$8.3 \times 10^2 - 10^4$	990-1010	90
Dutton 1989	Mafic recharge	10-30	Plag	74	sat.	2546-2556	80-88	1080-1180	200 ^b
Pinatubo 1991	Basalt	19-25	Plag (0.75) Hb+Aug+Ol (0.25)	73.2	2-3 usat.	2159-2169	$6.1 \times 10^2 - 6.7 \times 10^2$	1250	250
Usu 1663	Mafic	0-1	Plag	54	n.u.	2351-2364	57-98	1000-1050	n.u.

797 ^a Calculated from bulk values given in the reference(s).

798 ^b Assumed value.

799 **Supplementary references:**

800

- 801 Barclay, J., Rutherford, M.J., Carroll, M.R., Murphy, M.D., Devine, J.D., Gardner, J., Sparks, R.S.J., 1998.
 802 Experimental phase equilibria constraints on pre-eruptive storage conditions of the Soufriere Hills
 803 magma. *Geophys. Res. Lett.* 25, 3437–3440.
- 804 Benyahia, S., Syamlal, M., O'Brien, T.J., 2012. Summary of MFIX equations 2012-1. URL <https://doi.org/10.1093/ps/psw001>
 805 GovdocumentationMFIXEquations2012-1 Pdf.
- 806 Bernard, A., Knittel, U., Weber, B., Weis, D., Albrecht, A., Hattori, K., Klein, J., Oles, D., 1996. Petrology and
 807 geochemistry of the 1991 eruption products of Mount Pinatubo (Luzon, Philippines) 1126.
- 808 Browne, B.L., Eichelberger, J.C., Patino, L.C., Vogel, T.A., Dehn, J., Uto, K., Hoshizumi, H., 2006. Generation of
 809 Porphyritic and Equigranular Mafic Enclaves During Magma Recharge Events at Unzen Volcano, Japan. *J.*
 810 *Petrol.* 47, 301–328. <https://doi.org/10.1093/ps/psw001>
- 811 Cadoux, A., Scaillet, B., Druitt, T.H., Deloule, E., 2014. Magma Storage Conditions of Large Plinian Eruptions of
 812 Santorini Volcano (Greece). *J. Petrol.* 55, 1129–1171. <https://doi.org/10.1093/ps/psw001>
- 813 Camus, G., Gourgaud, A., Vincent, P.M., 1987. Petrologic evolution of Krakatau (Indonesia): Implications for a
 814 future activity. *J. Volcanol. Geotherm. Res.* 33, 299–316. [https://doi.org/10.1016/0377-0273\(87\)90020-5](https://doi.org/10.1016/0377-0273(87)90020-5)
- 815 Cioni, R., Civetta, L., Marianelli, P., Metrich, N., Santacroce, R., Sbrana, A., 1995. Compositional layering and syn-
 816 eruptive mixing of a periodically refilled shallow magma chamber: the AD 79 Plinian eruption of Vesuvius.
 817 *J. Petrol.* 36, 739–776.
- 818 Coombs, M.L., Eichelberger, J.C., Rutherford, M.J., 2000. Magma storage and mixing conditions for the 1953-74
 819 eruptions of Southwest Trident volcano, Katmai National Park, Alaska. *Contrib. Mineral. Petrol.* 140, 99–
 820 118.
- 821 Coombs, M.L., Eichelberger, J.C., Rutherford, M.J., 2002. Experimental and textural constraints on mafic enclave
 822 formation in volcanic rocks. *J. Volcanol. Geotherm. Res.* 119, 125–144.
- 823 Coombs, M.L., Gardner, J.E., 2001. Shallow-storage conditions for the rhyolite of the 1912 eruption at Novarupta,
 824 Alaska. *Geology* 29, 775–778.
- 825 Cottrell, E., Gardner, J.E., Rutherford, M.J., 1999. Petrologic and experimental evidence for the movement and
 826 heating of the pre-eruptive Minoan rhyodacite (Santorini, Greece). *Contrib. Mineral. Petrol.* 135, 315–
 827 331.
- 828 Couch, S., Sparks, R.S.J., Carroll, M.R., 2001. Mineral disequilibrium in lavas explained by convective self-mixing in
 829 open magma chambers. *Nature* 411, 1037–1039.
- 830 Cui, X., Li, J., Chan, A., Chapman, D., 2014. Coupled DEM-LBM simulation of internal fluidisation induced by a
 831 leaking pipe. *Powder Technol.* 254, 299–306. <https://doi.org/10.1016/j.powtec.2014.01.048>
- 832 Druitt, T.H., 2014. New insights into the initiation and venting of the Bronze-Age eruption of Santorini (Greece),
 833 from component analysis. *Bull. Volcanol.* 76, 794. <https://doi.org/10.1007/s00445-014-0794-x>
- 834 Druitt, T.H., Edwards, L., Mellors, R.M., Pyle, D.M., Sparks, R.S.J., Lanphere, M., Davies, M., Barreiro, B., 1999.
 835 Santorini Volcano. *Geol. Soc. Mem.* 19, 165.
- 836 Eichelberger, J.C., Izbekov, P.E., 2000. Eruption of andesite triggered by dyke injection: contrasting cases at
 837 Karymsky Volcano, Kamchatka and Mt Katmai, Alaska. *Philos. Trans. RS Lond.* A358, 1465–1485.
- 838 Ergun, S., 1952. Fluid flow through packed columns. *Chem Eng Prog* 48, 89–94.
- 839 Flaherty, T., Druitt, T.H., Tuffen, H., Higgins, M.D., Costa, F., Cadoux, A., 2018. Multiple timescale constraints for
 840 high-flux magma chamber assembly prior to the Late Bronze Age eruption of Santorini (Greece). *Contrib.*
 841 *Mineral. Petrol.* 173, 75. <https://doi.org/10.1007/s00410-018-1490-1>
- 842 Garg, R., Galvin, J., Li, T., Pannala, S., 2010. Documentation of open-source MFIX-DEM software for gas-solids
 843 flows. URL <https://doi.org/10.1093/ps/psw001> Accessed 31 March 2014.
- 844 Gidaspow, D., 1986. Hydrodynamics of Fluidization and Heat Transfer: Supercomputer Modeling. *Appl. Mech. Rev.*
 845 39, 1–23. <https://doi.org/10.1115/1.3143702>
- 846 Hammer, J.E., Rutherford, M.J., Hildreth, W., 2002. Magma storage prior to the 1912 eruption at Novarupta,
 847 Alaska. *Contrib. Mineral. Petrol.* 144, 144–162.

- 848 Holtz, F., Sato, H., Lewis, J., Behrens, H., Nakada, S., 2005. Experimental petrology of the 1991-1995 Unzen dacite,
849 Japan. Part I. Phase relations, phase composition and pre-eruptive conditions. *J. Petrol.* 46, 319–337.
- 850 Humphreys, M.C.S., Edmonds, M., Christopher, T., Hards, V., 2010. Magma hybridisation and diffusive exchange
851 recorded in heterogeneous glasses from Soufrière Hills Volcano, Montserrat. *Geophys. Res. Lett.* 37.
- 852 Izbekov, P., Gardner, J.E., Eichelberger, J.C., 2004. Comagmatic granophyre and dacite from Karymsky volcanic
853 center, Kamchatka: experimental constraints for magma storage conditions. *J. Volcanol. Geotherm. Res.*
854 131, 1–18.
- 855 Izbekov, P.E., Eichelberger, J.C., Patino, L.C., Vogel, T.A., Ivanov, B.V., 2002. Calcic cores of plagioclase phenocrysts
856 in andesite from Karymsky volcano: Evidence for rapid introduction by basaltic replenishment. *Geology*
857 30, 799–802. [https://doi.org/10.1130/0091-7613\(2002\)030<0799:CCOPPI>2.0.CO;2](https://doi.org/10.1130/0091-7613(2002)030<0799:CCOPPI>2.0.CO;2)
- 858 Kilgour, G., Blundy, J., Cashman, K., Mader, H.M., 2013. Small volume andesite magmas and melt–mush
859 interactions at Ruapehu, New Zealand: evidence from melt inclusions. *Contrib. Mineral. Petrol.* 166, 371–
860 392. <https://doi.org/10.1007/s00410-013-0880-7>
- 861 Mandeville, C.W., Carey, S., Sigurdsson, H., 1996. Magma mixing, fractional crystallization and volatile degassing
862 during the 1883 eruption of Krakatau volcano, Indonesia. *J. Volcanol. Geotherm. Res.* 74, 243–274.
- 863 Miller, T.P., Chertkoff, D.G., Eichelberger, J.C., Coombs, M.L., 1999. Mount Dutton volcano, Alaska: Aleutian arc
864 analog to Unzen volcano, Japan. *J. Volcanol. Geotherm. Res.* 89, 275–301.
- 865 Murphy, M.D., Sparks, R.S.J., Barclay, J., Carroll, M.R., Brewer, T.S., 2000. Remobilization of andesite magma by
866 intrusion of mafic magma at the Soufriere Hills Volcano, Montserrat, West Indies. *J. Petrol.* 41, 21–42.
- 867 Nakagawa, M., Wada, K., Thordarson, T., Wood, C.P., Gamble, J.A., 1999. Petrologic investigations of the 1995 and
868 1996 eruptions of Ruapehu volcano, New Zealand: formation of discrete and small magma pockets and
869 their intermittent discharge. *Bull. Volcanol.* 61, 15–31.
- 870 Nakagawa, M., Wada, K., Wood, C.P., 2002. Mixed magmas, mush chambers and eruption triggers: Evidence from
871 zoned clinopyroxene phenocrysts in andesitic scoria from the 1995 eruptions of Ruapehu volcano, New
872 Zealand. *J. Petrol.* 43, 2279–2303.
- 873 Nye, C.J., Swanson, S.E., Avery, V.F., Miller, T.P., 1994. Geochemistry of the 1989-1990 eruption of Redoubt
874 volcano: Part I. Whole-rock major- and trace-element chemistry. *J. Volcanol. Geotherm. Res.* 62, 429–452.
- 875 Pallister, J.S., Hoblitt, R.P., Meecker, G.P., Knight, R.J., Siems, D.F., 1996. Magma mixing at Mount Pinatubo:
876 petrographic and chemical evidence from the 1991 deposits. pp. 687–731.
- 877 Pallister, J.S., Hoblitt, R.P., Reyes, A.G., 1992. A basalt trigger for the 1991 eruptions of Pinatubo volcano ? *Nature*
878 356, 426–428.
- 879 Pichavant, M., Poussineau, S., Lesne, P., Solaro, C., Bourdier, J.-L., 2018. Experimental Parametrization of Magma
880 Mixing: Application to the ad 1530 Eruption of La Soufrière, Guadeloupe (Lesser Antilles). *J. Petrol.* 59,
881 257–282. <https://doi.org/10.1093/petrology/egy030>
- 882 Plail, M., Edmonds, M., Woods, A.W., Barclay, J., Humphreys, M.C.S., Herd, R.A., Christopher, T., 2018. Mafic
883 enclaves record syn-eruptive basalt intrusion and mixing. *Earth Planet. Sci. Lett.* 484, 30–40.
884 <https://doi.org/10.1016/j.epsl.2017.11.033>
- 885 Scaillet, B., Pichavant, M., Cioni, R., 2008. Upward migration of Vesuvius magma chamber over the past 20,000
886 years. *Nature* 455, 216–220.
- 887 Self, S., 1992. Krakatau revisited: The course of events and interpretation of the 1883 eruption. *GeoJournal* 28,
888 109–121. <https://doi.org/10.1007/BF00177223>
- 889 Shi, Y.F., Yu, Y.S., Fan, L.T., 1984. Incipient fluidization condition for a tapered fluidized bed. 484–489.
- 890 Singer, B.S., Costa, F., Herrin, J.S., Hildreth, W., Fierstein, J., 2016. The timing of compositionally-zoned magma
891 reservoirs and mafic ‘priming’ weeks before the 1912 Novarupta-Katmai rhyolite eruption. *Earth Planet.*
892 *Sci. Lett.* 451, 125–137. <https://doi.org/10.1016/j.epsl.2016.07.015>
- 893 Swanson, S.E., Nye, C.J., Miller, T.P., Avery, V.F., 1994. Geochemistry of the 1989-1990 eruption of Redoubt
894 volcano: Part II. Evidence from mineral and glass chemistry. *J. Volcanol. Geotherm. Res.* 62, 453–468.
- 895 Syamlal, M., Rogers, W., OBrien, T.J., 1993. MFIX documentation theory guide. USDOE Morgantown Energy
896 Technology Center, WV (United States).
- 897 Takahashi, R., Nakagawa, M., 2013. Formation of a Compositionally Reverse Zoned Magma Chamber: Petrology of
898 the ad 1640 and 1694 Eruptions of Hokkaido-Komagatake Volcano, Japan. *J. Petrol.* 54, 815–838. <https://doi.org/10.1093/petrology/egs087>
- 899

- 900 Tomiya, A., Takahashi, E., 2005. Evolution of the Magma Chamber beneath Usu Volcano since 1663: a Natural
901 Laboratory for Observing Changing Phenocryst Compositions and Textures. *J. Petrol.* 46, 2395–2426.
902 <https://doi.org/10.1093/petrology/egi057>
- 903 Vetere, F., Behrens, H., Schuessler, J.A., Holtz, F., Misiti, V., Borchers, L., 2008. Viscosity of andesite melts and its
904 implication for magma mixing prior to Unzen 1991–1995 eruption. *J. Volcanol. Geotherm. Res., Scientific*
905 *drilling at Mount Unzen* 175, 208–217. <https://doi.org/10.1016/j.jvolgeores.2008.03.028>
- 906 Wolf, K.J., Eichelbeger, J.C., 1997. Syneruptive mixing, degassing, and crystallization at Redoubt Volcano, eruption
907 of December, 1989 to May 1990. *J. Volcanol. Geotherm. Res.* 75, 19–37.
- 908
- 909